

Surprising Properties of Static and Flowing Granular Matter

by

MOHAMMAD YASINUL KARIM

A DISSERTATION

Presented to the Department of Physics  
and the Graduate School of the University of Oregon  
in partial fulfillment of the requirements  
for the degree of  
Doctor of Philosophy

June 2017

## DISSERTATION APPROVAL PAGE

Student: Mohammad Yasinul Karim

Title: Surprising Properties of Static and Flowing Granular Matter

This dissertation has been accepted and approved in partial fulfillment of the requirements for the Doctor of Philosophy degree in the Department of Physics by:

Richard Taylor	Chair
Eric Corwin	Advisor
Benjamin McMorran	Core Member
Marina Guenza	Institutional Representative

and

Original approval signatures are on file with the University of Oregon Graduate School.

Degree awarded June 2017

© 2017 Mohammad Yasinul Karim

This work is licensed under a Creative Commons

**Attribution-NonCommercial-NoDerivs (United States) License.**



## DISSERTATION ABSTRACT

Mohammad Yasinul Karim

Doctor of Philosophy

Department of Physics

June 2017

Title: Surprising Properties of Static and Flowing Granular Matter

The Janssen effect is a unique property of confined granular materials experiencing gravitational compaction in which the bottom pressure saturates with increasing filling height due to frictional interactions with side walls. By replacing gravitational compaction with frictional compaction on a horizontal conveyor belt, we study friction-compacted 2D granular materials confined within fixed boundaries. Even with high-friction side walls the Janssen effect completely vanishes. Our results demonstrate that gravity-compacted granular systems are inherently different from friction-compacted systems in at least one important way: vibrations induced by sliding friction with the driving surface relax away tangential forces on the walls. Remarkably, we find that the Janssen effect can be recovered by replacing the straight side walls with a sawtooth pattern. The mechanical force introduced by varying the sawtooth angle  $\theta$  can be viewed as equivalent to a tunable friction force. By construction, this mechanical friction force cannot be relaxed away by vibrations in the system. This work is described in Chapter II and has been published in *Physical Review Letters*.

We experimentally study quasi-2d dilute granular flow around intruders whose shape, size and impact speeds are systematically varied. Direct measurement of the flow field reveals that three in-principle independent measurements of the non-uniformity of the flow field are in fact all linearly related: 1) granular temperature, 2) flow field divergence and 3) shear-strain rate. The shock front is defined as the local maxima in each measurement. The shock front is well described by an inverted catenary and is driven by the formation of a dynamic arch during steady flow. We find universality in the functional form of the shock front within the range of experimental values probed. Changing the intruder size, concavity and impact speed only results in a scaling and shifting of the shock front. We independently measure the horizontal lift force on the intruder and

find that it can be understood as a result of the interplay between the shock profile and intruder shape.

This dissertation includes previously published and unpublished co-authored material.

## CURRICULUM VITAE

NAME OF AUTHOR: Mohammad Yasinul Karim

### GRADUATE AND UNDERGRADUATE SCHOOLS ATTENDED:

University of Oregon, Eugene, OR  
Reed College, Portland, OR

### DEGREES AWARDED:

Doctor of Philosophy, Physics, 2017, University of Oregon  
Bachelor of Arts, Physics, 2010, Reed College

### AREAS OF SPECIAL INTEREST:

Soft Condensed Matter  
Non-equilibrium Physics  
Biophysics

### PROFESSIONAL EXPERIENCE:

Research Assistant, Physics, University of Oregon, 2012-2017

Teaching Assistant, Physics, University of Oregon, 2010-2012, 2015, 2016

Teaching Assistant, Physics, Reed College, 2006-2010

### PUBLICATIONS:

M. Yasinul Karim, E. I. Corwin. “Eliminating friction with friction.” *Physical Review Letters* (2014).

## ACKNOWLEDGEMENTS

I owe a huge debt of gratitude to Eric Corwin for his guidance and patience. Without his brilliant input this work would not have been possible. Thank you for everything Eric!

## TABLE OF CONTENTS

Chapter	Page
I. INTRODUCTION . . . . .	1
II. 2D JANSSEN EFFECT IN A FRICTION-DRIVEN SYSTEM . . . . .	4
Background . . . . .	4
Results and Discussion . . . . .	9
III. UNIVERSALITY IN GRANULAR SHOCK FRONTS ABOVE AN INTRUDER . . . . .	14
Background . . . . .	14
Results and Discussion . . . . .	18
IV. SUPPLEMENTARY MATERIALS FOR CHAPTER III . . . . .	24
Forces on Grain Pile . . . . .	24
V. CONCLUSION . . . . .	30
REFERENCES CITED . . . . .	33

## LIST OF FIGURES

Figure	Page
1. Diagram of the experimental setup. The nickels are driven by the belt into a 2D container that is stationary. The nickels are blocked at one end by an acrylic barrier which presses against two force sensors A and B as the nickels accumulate against this surface. The nickels are confined on the sides by walls constructed from ABS and with sawtooth patterns engraved on the sides facing the nickels. The arrow points towards direction of conveyor belt. . . . .	5
2. Measured force ( $F$ ) per container width ( $w$ ) is plotted at various filling heights for $\theta = 0^\circ, 5^\circ, 7.5^\circ, 10^\circ, 15^\circ, 20^\circ, 30^\circ, 40^\circ, 45^\circ$ and $90^\circ$ . The data is fitted to the equation $F/w = \mu\rho g\eta(1 - \exp(-x/\eta))$ (solid lines). The bottom pressure ( $F/w$ ) saturates faster with increasing angle of inclination of the triangles along the side walls. At very low angles of inclination ( $\theta = 0^\circ, 5^\circ, 7.5^\circ$ ) the bottom pressure increases nearly linearly for the observed filling heights. . . . .	8
3. The dimensionless quantity $F/(wg\eta)$ is plotted against $x/\eta$ for several values of $\theta$ and all data collapses onto a single master curve given by $F/(wg\eta) = 1 - \exp(-x/\eta)$ . Inset is a plot of fitted values of width versus angle of inclination $\theta$ . . . . .	10
4. Fitted values of characteristic filling height per container width is plotted against various angles of inclination. The data is fitted to our model of $\eta$ as a function of the angle of inclination $\theta$ , as described in equation. Inset is an illustration of the interaction of forces necessary to create a mechanical friction that increases with increasing $\theta$ . Consequently higher $\theta$ leads to lower $\eta$ . . . . .	11
5. a) Front view of experimental setup. The intruder in the picture corresponds to a super-disk exponent $n = 7.5$ . b) Intruder-sensor system schematic. c) Examples of intruders with different super-disk exponents. As $n$ increases the shapes become more convex with $n = \infty$ being a square. . . . .	15
6. a-c) Intensity plot of scaled granular temperature, absolute divergence of the flow field, and local shear-strain rate for $n = 0.75$ . d - f) Scatter plots of scaled flow-field divergence versus temperature, flow field divergence versus local shear rate, and shear rate versus temperature respectively, measured from all points enclosed by the white dotted regions. . . . .	16

Figure	Page
7. a) Plots of shock fronts. Scaled $x$ and $y$ coordinates are in units of $R$ , the vertical length of the intruder. The data is shown for $n = 0, 0.75, 0.85, 0.95, 1, 1.5, 2, 2.5, 5, 7.5, 10, \infty$ . Solid black lines are fits to Equation 3.5. b) Plot of scaled shock boundaries for all probed values of $n$ with constant $R = 4$ inches shown in circles. Squares represent all tested intruder locations $h \in \{23, 34, 46, 57, 69, 84\}$ cm and intruder radii, $R \in \{2, 3, 4, 7\}$ inches for constant $n = 2$ . Diamond symbols represent data from an asymmetric intruder with random features on it (shown in Figure 2 of the Supplement). The black curve is the inverted catenary given by Equation 3.5. c) Top to bottom - plots of the fit parameters $w$ , $c$ and $w + p$ as functions of $n$ respectively. Red circles represent data from varying $n$ with constant $R$ and blue squares represent data from fixed $n = 2$ but different combinations of $R$ and impact speed $v_0$ . The dashed line shows the mean width $ \bar{w}  \approx 0.8$ . In the $c$ versus $n$ plot the dark solid curve shows center of mass of the intruders shifts with varying $n$ .	20
8. a) Plot of horizontal lift forces from force sensor (green circle) and calculated lift forces (dark blue squares) as a function of $n$ . Lift is maximum for $n \rightarrow 0$ and decreases to 0 as $n \rightarrow \infty$ . Inset is an illustration showing the intruder, outlined in black, trapped grains, in grey and shock profile in red. The solid green arrow represents the tangential net force $\vec{F}(s, \theta)$ on a small segment of the shock front. Dotted green arrows are components of this vector. Purple arrows labeled $v_{x,0/1}$ represent horizontal ejected grain velocities from the trapped region. b) Plot of the left (red) and right (blue) exit heights $l$ as a function of $n$ . c) Plot of absolute horizontal left (red) and right (blue) exit velocities $ v_x $ versus $n$ .	21
9. Diagram of force vectors and velocities used to calculate $F_L$ .	26
10. Illustration of the intruder with random features on the leading edge. The shock front from this shape still maintains the catenary shape.	27
11. Plots of total measured lift force $F_{meas}$ , calculated lift force $F_L$ (blue squares), force due to mass ejection from trapped pile $F_{flow}$ (green diamond), quasi-static load contribution $F_S$ (downward pointing arrow), and force due to impacts $F_C$ (upward pointing arrow) as a function of $n$ .	28
12. Representative mean flow field around an intruder with super-disk exponent $n = 0.75$ . The white masked out region is the intruder and the arrows are velocity vectors.	29

## CHAPTER I

### INTRODUCTION

Leaving aside the impetus of human curiosity for a moment, the ubiquity and commercial relevance of granular materials dictate that we understand the properties of these fascinating systems. From the sands on a beach [1] to the surface of Mars [2], from food grains to the rocky rings of Saturn [3, 4], nature is full of these materials we describe as granular [5, 6].

The term granular materials describes a class of matter that has a characteristic energy scale far exceeding  $k_B T$ , where  $k_B$  is the Boltzmann constant and  $T$  being ambient temperature. Consequently, changes in ambient temperature do little to alter the properties of a granular system. So, for instance, changes in temperature along the Oregon coast do not directly result in a rearrangement of its sandy beaches. But temperature fluctuations do account for the complex and often unpredictable weather patterns experienced there. In other words, granular materials stand in stark contrast to gases and liquids where thermal effects lead to changes in the state of the system. Instead of  $k_B T$ , the characteristic energy scale in a granular system is set by  $mgd$  where  $m$  is the mass of a constituent particle,  $g$  the acceleration due to gravity and  $d$  the characteristic size of the particle. Here,  $mgd$  can be thought of as the energy required for one grain to move past another.

The temperature independence of granular systems makes them no less complicated than fluids. The presence of dissipative forces like friction and deformation give rise to further complexity but also to a vast array of phenomena that make these systems very interesting. For example, in a vibrated granular system with particles of different sizes but equal densities there are convective flows that lead to size segregation of particles, commonly referred to as the Brazil nut effect [7, 8]. The bigger (heavier) particles are pushed to the top as the smaller particles get jostled around to fill voids.

Even static granular systems exhibit behaviors that defy expectations. One such example is the Janssen effect named after H. A. Janssen, a German engineer. In 1895 Janssen wrote down a mathematical description for the pressure at the bottom of a container filled with grains [9]. It was already known that a silo full of corn husks for instance, does not obey Stevin's law which tells us that the pressure at the base due to a column of liquid is proportional to the height of

liquid from the base to the surface. In the case of a static granular system the pressure at the base saturates with increasing filling height. This happens due to the formation of more robust force distribution networks that redirect the increased weight from added grains to the container side-walls rather than the base. This redistribution of the load is facilitated by grain-grain and grain-wall frictional forces.

Chapter II will focus on an experiment carried out to study this Janssen effect in two dimensions. The grains in this study were placed on a horizontal moving surface such that they were compacted by frictional forces and not gravity as was the case for Janssen's original study. We show in this study that Janssen's relation does not hold, shedding light on how grain-wall friction is crucial in establishing the force network necessary to redistribute load to the side-walls. In the presence of a slipping surface in the friction compacted case, the grains adjacent to the walls fail to maintain static frictional contact so the entire system suddenly behaves like a fluid, following Stevin's law. We further show that it is possible to suppress this fluid-like behavior and re-establish Janssen's relation by introducing a suitable wall geometry so that the static friction is replaced by a mechanical force that ultimately helps redirect increased load to the side-walls. The contents of Chapter II have been published as an article in Physical Review Letters [10]. This chapter is based on work that has been published in Physical Review Letters volume 112 on May 9, 2014. My adviser Eric Corwin is a co-author on the paper.

Chapter III delves into the physics of obstructed granular flow. In this study we looked at the connection between obstacle geometry, the granular shock front and lift forces on the obstacle. Whenever an object (e.g. a plane) moves through a medium (e.g. air) at a speed exceeding the speed of sound there is a shock front. As an example, for planes moving at less than the speed of sound, pressure waves are traveling faster than the plane itself so neighboring air molecules can rearrange in a continuous fashion. As the plane starts traveling at or faster than the speed of sound the information about the plane is no longer propagating fast enough. As a result the air around the plane becomes discontinuously compressed and this appears as a shock front. In air the angle of the cone forming the shock front depends on the speed of the object. Other factors such as the geometry of the bow and airfoils play a role in the complex shock waves around the plane.

For Chapter III, the system of an obstacle in flowing grains is analogous to a plane in air. For simplicity our experiment was conducted in a quasi-two dimensional system, meaning the thickness of the system is small enough that we can ignore it. Furthermore, the speed of sound in a low-density granular system is very low. This means an object moving at speeds of a few centimeters per second will experience a shock front. To vary the geometry in a systematic manner we generate the shapes from a set of curves defined by super-disks. This allows for the turning of a single knob to continuously vary geometry and study corresponding changes in the shock front and lift.

The results of this study demonstrate that while granular materials exhibit fluid-like behavior they possess properties that are unique to these systems. For instance, we find that the shock front maintains the same shape even with varying geometry and impact speeds. We show that grains pile up around the obstacle such that the front separating the nearly static grains from flowing grains is described by a unique shape that can be derived from force balance arguments with proper constraints. Our model for the shock front is a catenary, a function famously describing the shape of a chain hanging freely from two ends [11, 12].

## CHAPTER II

### 2D JANSSEN EFFECT IN A FRICTION-DRIVEN SYSTEM

This chapter includes work that has been published in Physical Review Letters volume 112 on May 9, 2014. The experimental design, data collection and analysis was done by me with guidance from my advisor, Eric Corwin, who is a co-author on the paper.

#### Background

The Janssen effect is a unique property of confined granular materials experiencing gravitational compaction in which the pressure at the bottom saturates with increasing filling height due to frictional interactions with side walls. In this paper we replace gravitational compaction with frictional compaction. We study friction-compacted 2D granular materials confined within fixed boundaries on a horizontal conveyor belt. We find that even with high friction side walls the Janssen effect completely vanishes. Our results demonstrate that gravity-compacted granular systems are inherently different from friction-compacted systems in at least one important way: vibrations induced by sliding friction with the driving surface relax away tangential forces on the walls. Remarkably, we find that the Janssen effect can be recovered by replacing the straight side walls with a sawtooth pattern. The mechanical force introduced by varying the sawtooth angle  $\theta$  can be viewed as equivalent to a tunable friction force. By construction, this mechanical friction force cannot be relaxed away by vibrations in the system.

This work was originally published in *Physical Review Letters*. The writing and analysis were performed by me as primary author. Eric Corwin is listed as a coauthor as he advised this work.

Granular materials in bulk can exhibit liquid-like, solid-like or gas-like behavior [6, 13–15]. There are few illustrations of this more striking than the Janssen effect in a grain-filled silo. The Janssen effect describes the saturation of bottom pressure with increasing filling height in a static 3D system of granular particles confined in a container with vertical walls [5, 9, 16]. If an empty silo is gradually filled with a frictional granular material a measurement at the bottom will initially show pressure increasing linearly with filling height. However, as the filling height becomes equal to the width of the silo the measured pressure at the bottom begins to

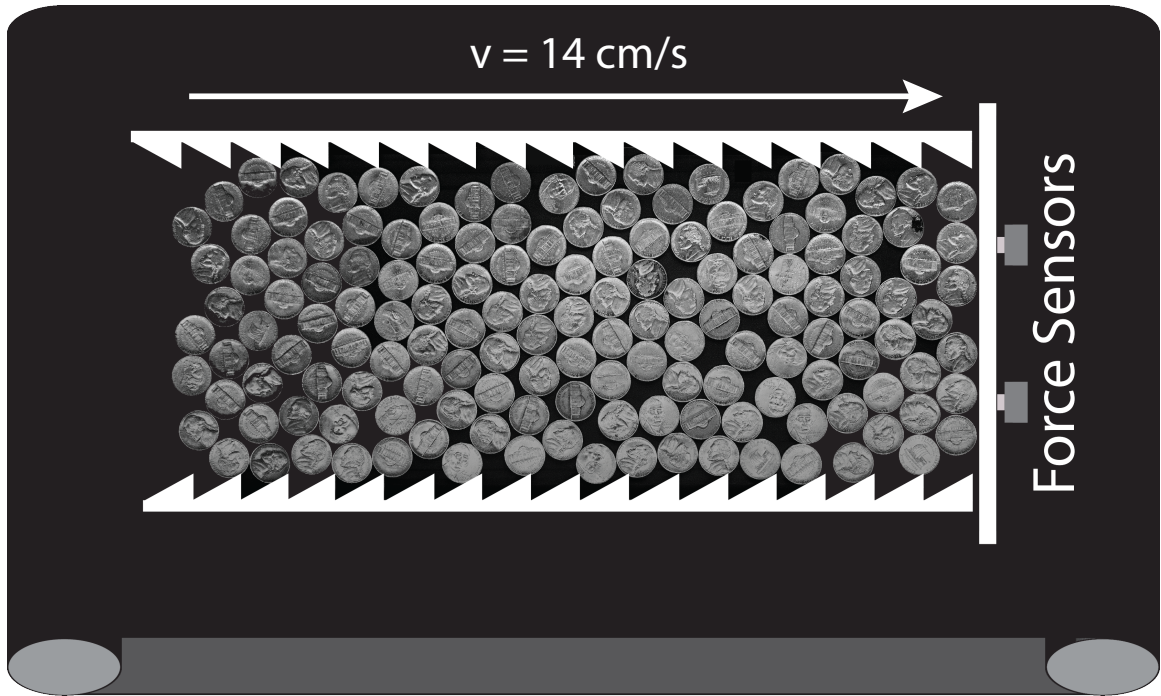


FIGURE 1. Diagram of the experimental setup. The nickels are driven by the belt into a 2D container that is stationary. The nickels are blocked at one end by an acrylic barrier which presses against two force sensors A and B as the nickels accumulate against this surface. The nickels are confined on the sides by walls constructed from ABS and with sawtooth patterns engraved on the sides facing the nickels. The arrow points towards direction of conveyor belt.

saturate, asymptoting to a constant value independent of filling height. As the granular material is compressed by the weight of the material above, it presses down on the material below and outwards on the confining walls. This creates a large normal force against the walls which allows for the mobilization of a large frictional tangential force between individual grains and the confining walls. Thus, in a tall silo the majority of the vertical force is actually borne by the walls of the silo. This is in striking contrast to a silo filled with liquid, in which the walls will only experience normal forces and thus carry none of the vertical load.

Vertical, gravity compacted 3D granular packings and granular hopper flows have been well studied [17–23]. However, industrial processes as diverse as coal mining, grain storage, oil extraction, and pharmaceutical manufacture, to name only a few, rely on granular materials being transported horizontally on conveyor belts. In recent works Aguirre, *et al.* have examined hopper flows in 2D granular systems where grains are loaded horizontally by a conveyor belt into a confining frame. They measured the flow rates of grains escaping through an aperture for

varying aperture sizes and belt speeds [24] and also the normal forces on the base during the granular discharge [25]. The results show that for a given aperture size, the hopper flow rate remains constant even though the pressure at the base changes as the grains leave the frame. They conclude that the Janssen effect, which in previous studies was invoked to explain the constant hopper flow rates, is irrelevant. Instead, the study shows that it is the local pressure near the aperture that determines the flow rate. However, they did not explore static packings and their experiments were limited to relatively short packings (ratio of maximum filling height to system width  $\approx 2$ ).

In this paper we present a direct investigation of the Janssen effect in confined 2D granular systems with no flow, compacted by dynamic friction. We find that in a 2D horizontal container with straight confining walls the pressure at the bottom increases linearly with filling height, demonstrating that the effective particle-wall friction is reduced to zero. Sawtooth walls have been used in 2D [26, 27] and 3D [28, 29] granular systems to tune the dynamic motion of grains in an excited system. Here we use them to change the boundary conditions of a static system. In this experiment we show that a sawtooth pattern can be employed in a static, friction-compacted granular system to recover a Janssen-like behavior.

We can write the expected Janssen equation for a 2D friction driven system by replacing the force of gravity with a downstream pointing dynamic friction force on each particle of  $\mu_{pb}mg$ , where  $\mu_{pb}$  is the coefficient of dynamic friction between a particle and the belt,  $m$  is the mass of a particle, and  $g$  is acceleration due to gravity. The 2D pressure  $F/w$ , where  $F$  is the total force at the bottom of the system and  $w$  is the effective width of the container, can be written as a function of the filling height  $x$  as

$$\frac{F}{w} = \mu_{pb}\rho g\eta(1 - \exp(-x/\eta)) \quad (2.1)$$

where  $\eta$  is the characteristic height for saturation of pressure and  $\rho$  is the 2D density.

In Janssen's calculation the normalized characteristic height  $\eta/w$  is

$$\frac{\eta}{w} = \frac{1}{2K\mu_{pw}} \quad (2.2)$$

where  $K$  is the ratio of horizontal pressure to vertical (downstream) pressure at any point in the granular system and  $\mu_{pw}$  is the particle-wall coefficient of friction. As in the gravity driven case, we make the simplifying assumption that  $K$  is constant throughout the entire system [5, 9, 16].

Figure 1 shows our experimental setup which consists of nickels in a horizontal 2D container on top of a 10 foot variable speed conveyor (McMaster-Carr 5900K786 with a Forbo Siegling PVC belt. We choose nickels as our granular particles due to their precise manufacture, large coefficient of friction, and their ability to resist buckling under compression. We measure the 2D bulk density of jammed nickels to be  $\simeq 11.45 \text{ kg/m}^2$ . The coefficient of dynamic friction between particles and the belt is measured to be  $\mu_{pb} \simeq 1$ . Our container consists of fixed sidewalls and a freely moving downstream barrier. The ends of the downstream barrier are mounted on rails so that the total force at the bottom of the packing can be measured by the two force sensors (Measurement Specialties FC22) and recorded digitally (National Instruments NI USB-6009). The sidewalls and the downstream barrier are held  $\simeq 0.25 \text{ mm}$  above the conveyor belt to prevent escape of the 1.95 mm tall nickels while avoiding contact between the belt and the walls. The sidewalls are 3D printed in ABS plastic for a range of sawtooth angles  $\theta$  using a Makerbot Replicator 2X. The repeat spacing of the sawtooth patterns is chosen to be 25.4 mm, slightly larger than the diameter of a nickel (21.21 mm). For each  $\theta$  we adjust the spacing of the sidewalls to maintain a constant increase in average filling height of 7.6 cm for every 30 nickels added. The effective width  $w$  of the system is calculated as a fit parameter from Equation 2.1 at each  $\theta$  and these values are plotted in Figure 3 inset.

For each  $\theta$  we measure the force at the downstream barrier as a function of filling height. We make each measurement by randomly distributing thirty nickels upstream on the conveyor belt and allowing them to come to rest within the container. After they have been deposited we record the average force  $F$  over a span of 30 s and directly measure the filling height  $x$ . We continue adding 30 nickels at a time and measuring the force until we reach a maximum filling height of 1.2 m or the nickels buckle. All measurements are taken with the belt moving at a constant a speed of 14 cm/s. This speed is slow enough that collisions don't result in buckling while still being fast enough for rapid data collection.

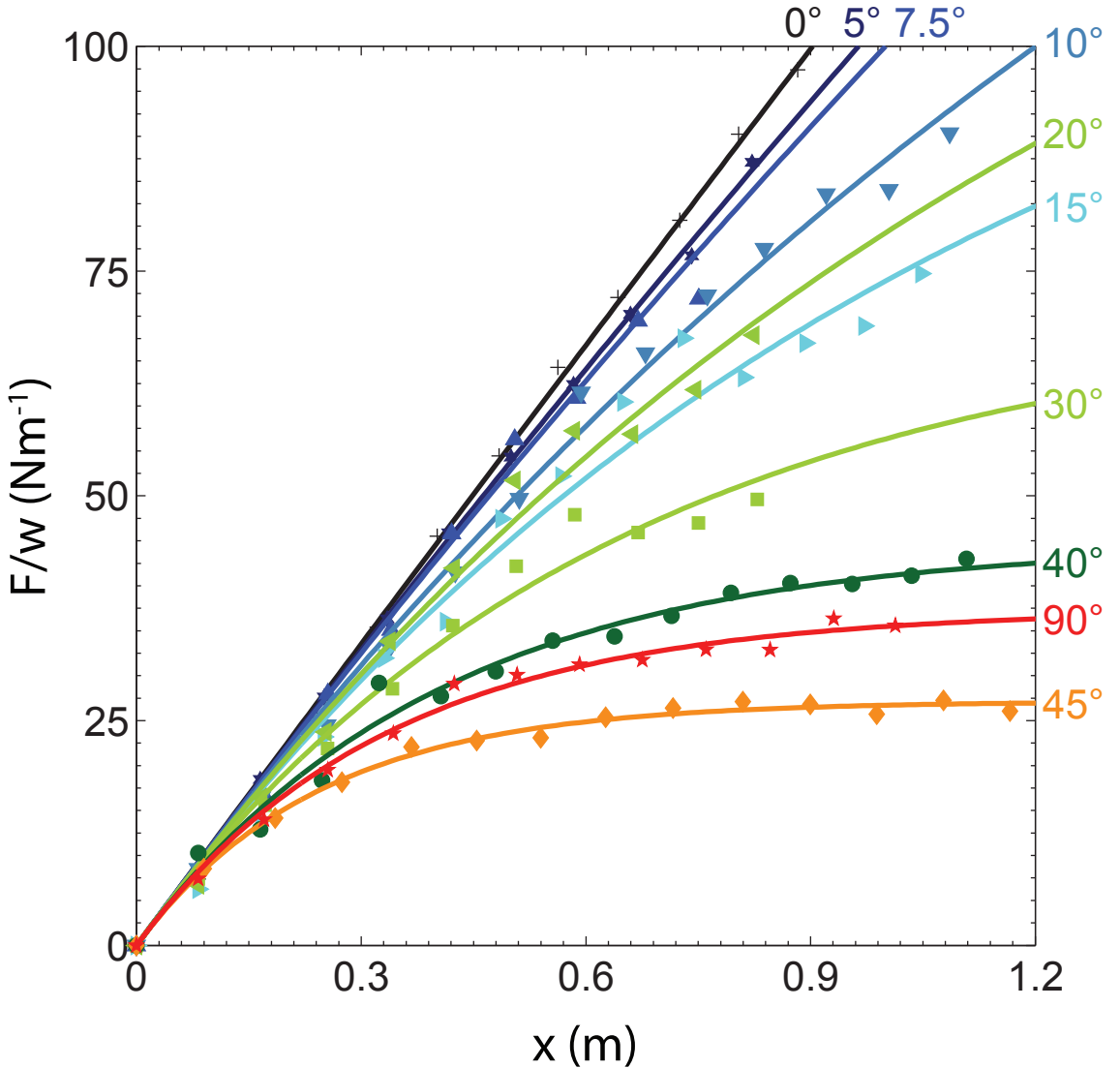


FIGURE 2. Measured force ( $F$ ) per container width ( $w$ ) is plotted at various filling heights for  $\theta = 0^\circ, 5^\circ, 7.5^\circ, 10^\circ, 15^\circ, 20^\circ, 30^\circ, 40^\circ, 45^\circ$  and  $90^\circ$ . The data is fitted to the equation  $F/w = \mu\rho g\eta(1 - \exp(-x/\eta))$  (solid lines). The bottom pressure ( $F/w$ ) saturates faster with increasing angle of inclination of the triangles along the side walls. At very low angles of inclination ( $\theta = 0^\circ, 5^\circ, 7.5^\circ$ ) the bottom pressure increases nearly linearly for the observed filling heights.

## Results and Discussion

Figure 2 presents experimental data along with 2-parameter fits to Equation 2.1. The fits yield values for characteristic height  $\eta$  and width  $w$ . We use the value of  $w$  to plot 2D pressure  $F/w$  as a function of filling height  $x$ . We find that for  $\theta = 0^\circ$  (straight walls) the 2D pressure  $F/w$  increases linearly with filling height, consistent with  $\eta = \infty$  and thus  $\mu_{pw} = 0$  (Figure 2). This is in striking contrast to the predicted scale of  $\eta$ , which would be of the order  $w$  for  $\mu_{pw}$  and  $K$  of the order 1. Thus, with straight walls, the high-friction granular system consisting of nickels seemingly behaves like a frictionless fluid. In the gravity-driven case, particle-wall friction is fully mobilized unless an outside force is introduced to the system. However, in our conveyor belt driven system, the constant sliding friction of the belt perturbs the nickels so that the particle-wall friction cannot be mobilized. Hence, we see the force of the granular system is completely borne by the base.

If we replace the straight walls with a sawtooth pattern, however, we recover Janssen-like behavior:  $F/w$  initially increases linearly with filling height and then bends over to a plateau for higher filling heights (Figure 2). The plateau value of the 2D pressure decreases with increasing  $\theta$ , even though the same perturbative sliding friction exists in the system. We demonstrate that our modified Janssen equation (Equation 2.1) accurately models the physics of the system by plotting a scaled pressure,  $F/(w\mu g \rho \eta)$  versus a scaled filling height,  $x/\eta$ , as shown in Figure 3.

Figure 3 demonstrates that the sidewalls are bearing much of the downstream force of the system, even in the absence of friction between the particles and the wall. Instead, this force must have a geometric origin. To account for this we can modify Equation 2.2 to relate the characteristic height to the geometrically determined downstream force on the sidewalls.

The emergence of Janssen-like behavior with sawtooth walls suggests that the geometry of the sidewalls allows them to support the load of the granular materials, even in the absence of friction with the particles. If we continue to assume that we have a fixed  $K$  relating the horizontal and vertical pressure then we can resolve the vertical force on the sawtooth sidewall as a geometric construction (Inset to Figure 4). A particle pressed against a sawtooth experiences an average net force,  $F_{net}$ , from the particles around it and the conveyor belt. This can be decomposed into horizontal  $F_h$  and vertical  $F_v$  components related by  $F_h = KF_v$ . To balance

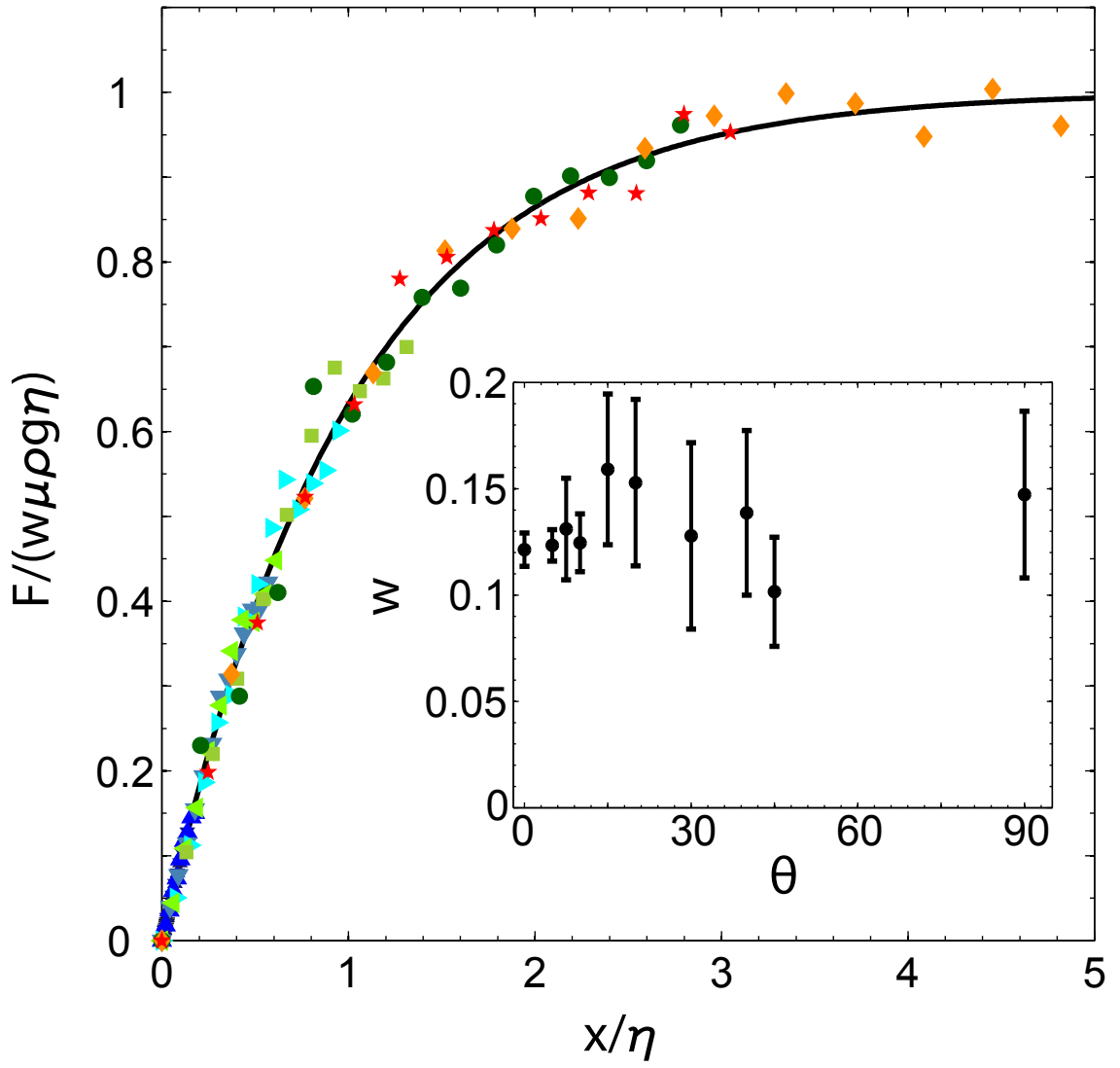


FIGURE 3. The dimensionless quantity  $F/(wg\rho\eta)$  is plotted against  $x/\eta$  for several values of  $\theta$  and all data collapses onto a single master curve given by  $F/(wg\rho\eta) = 1 - \exp(-x/\eta)$ . Inset is a plot of fitted values of width versus angle of inclination  $\theta$ .

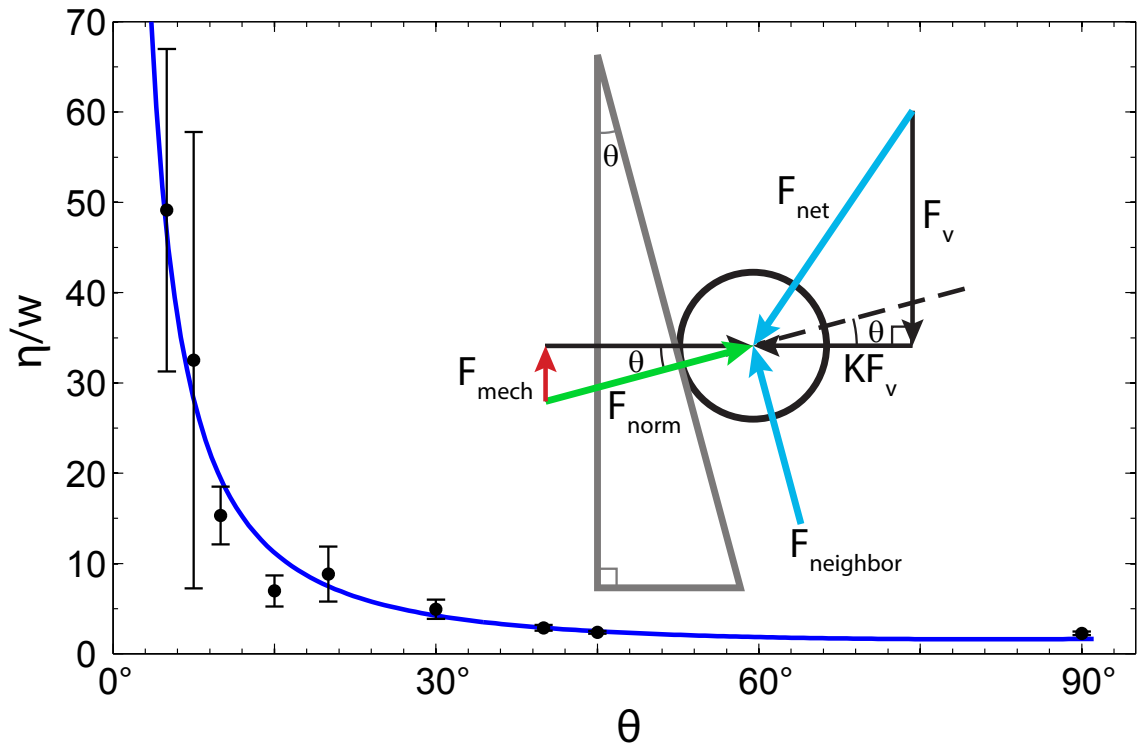


FIGURE 4. Fitted values of characteristic filling height per container width is plotted against various angles of inclination. The data is fitted to our model of  $\eta$  as a function of the angle of inclination  $\theta$ , as described in equation. Inset is an illustration of the interaction of forces necessary to create a mechanical friction that increases with increasing  $\theta$ . Consequently higher  $\theta$  leads to lower  $\eta$ .

the forces on a particle pressed against the wall the sawtooth must exert a normal force of

$$F_{norm} = F_{net} \frac{K \cos \theta + \sin \theta}{\sqrt{K^2 + 1}} \quad (2.3)$$

(green arrow in Figure 4 inset) and the particle below it must provide a force  $F_{neighbor}$ . We can in turn decompose  $F_{norm}$  to find the vertical reaction force

$$F_{mech} = F_{net} \frac{(K/2) \sin 2\theta + \sin^2 \theta}{\sqrt{K^2 + 1}} \quad (2.4)$$

(red vector). Since in the original formulation  $\mu_{pw}$  serves to create a vertical reaction force in the walls we can redefine Equation 2.2 as

$$\frac{\eta}{w} = \frac{F_{net}}{2KF_{mech}} = \frac{\sqrt{K^2 + 1}}{K(K \sin 2\theta + 2 \sin^2 \theta)}. \quad (2.5)$$

We plot  $\eta/w$  as a function of  $\theta$  in Figure 4. We find that Equation 2.5 well fits this data for all values of  $\theta$  with a single fit parameter  $K = 0.32 \pm 0.02$ . This value of  $K$  indicates that the horizontal forces on the confining walls are  $\simeq 1/3$  of the vertical forces that are directed to the bottom. Experimental studies of 3D gravity compacted granular materials reported values in the range 0.2-0.8 dependent on measurement technique, material, and filling protocol [9, 30–33]. As done in these studies, we have also employed the approximation that the stress ratio is constant. The fact that our data is well fit by a single parameter,  $K$ , which falls within this range suggests that our approximation is valid.

In this paper we have shown that vibrations due to dynamic friction in conveyor belt driven systems is sufficient to relax away tangential forces on straight side walls. Under such conditions, a granular system behaves like a hydrostatic system; the pressure at the bottom increases linearly with filling height. However, a Janssen effect can be recovered if we use sawtooth walls to introduce mechanical friction. We find that the dependence of saturation height on the angle of the sawtooth is well modeled by simple geometric arguments.

These results have direct application to industrial processes involving the transport and containment of granular materials on conveyor belts. Our results show that large stresses in high friction granular systems can be reduced by modifying the confining wall geometry. By

reducing the interparticle stress one should observe a reduced probability of buckling in the system. Further, a lower interparticle stress should reduce the energy required to break up a jammed system and lead to smoother flowing transport of material.

While this study sheds light on the role of geometry in static, friction-compacted granular systems, the next chapter delves into its role in gravity-driven, obstructed granular flows in similarly quasi-two dimensional systems. More specifically, the study focuses on the nature of shock waves in granular flows around an obstruction whose geometry is varied systematically. Much like this study, Chapter III will take an experimental approach to study quasi 2D granular systems, but this time in flow.

## CHAPTER III

### UNIVERSALITY IN GRANULAR SHOCK FRONTS ABOVE AN INTRUDER

#### Background

This chapter includes work that has not yet been published but submitted to Physical Review E. The experimental design, data collection and analysis was done by me with guidance from my advisor, Eric Corwin, who is a co-author on the paper.

We experimentally study quasi-2d dilute granular flow around intruders whose shape, size and relative impact speed are systematically varied. Direct measurement of the flow field reveals that three in-principle independent measurements of the non-uniformity of the flow field are in fact all linearly related: 1) granular temperature, 2) flow field divergence and 3) shear-strain rate. The shock front is defined as the local maxima in each of these measurements. The shape of the shock front is well described by an inverted catenary and is driven by the formation of a dynamic arch during steady flow. We find universality in the functional form of the shock front within the range of experimental values probed. Changing the intruder size, concavity and impact speed only results in a scaling and shifting of the shock front. We independently measure the horizontal lift force on the intruder and find that it can be understood as a result of the interplay between the shock profile and the intruder shape.

Lift forces [34–37] on and shock formation [38–40] around intruders in granular flows are well known phenomena. Rericha *et al.* [39] and Boudet *et al.* [41, 42] have demonstrated that shocks analogous to those in fluid flows are formed around symmetrical intruders in dilute granular flows. Numerical studies by Potiguar [36] have shown that in the case of asymmetrical intruders the drag-induced lift forces are lower than expected due to the formation of shock waves that act as a shield. However, the relationship between the granular shock front and lift (forces perpendicular to the direction of flow) on an intruder has not been studied in detail.

In this letter we systematically vary the shape of an intruder in a dilute granular flow and measure the resulting grain flow fields and lift forces. We find that the position of the shock front is well-described by each of the coordinates of the local maxima of granular temperature, divergence, and local shear-strain rate, which are all found to be linearly related. The shock front maintains a symmetric shape and its center point closely tracks the center of mass of the intruder.

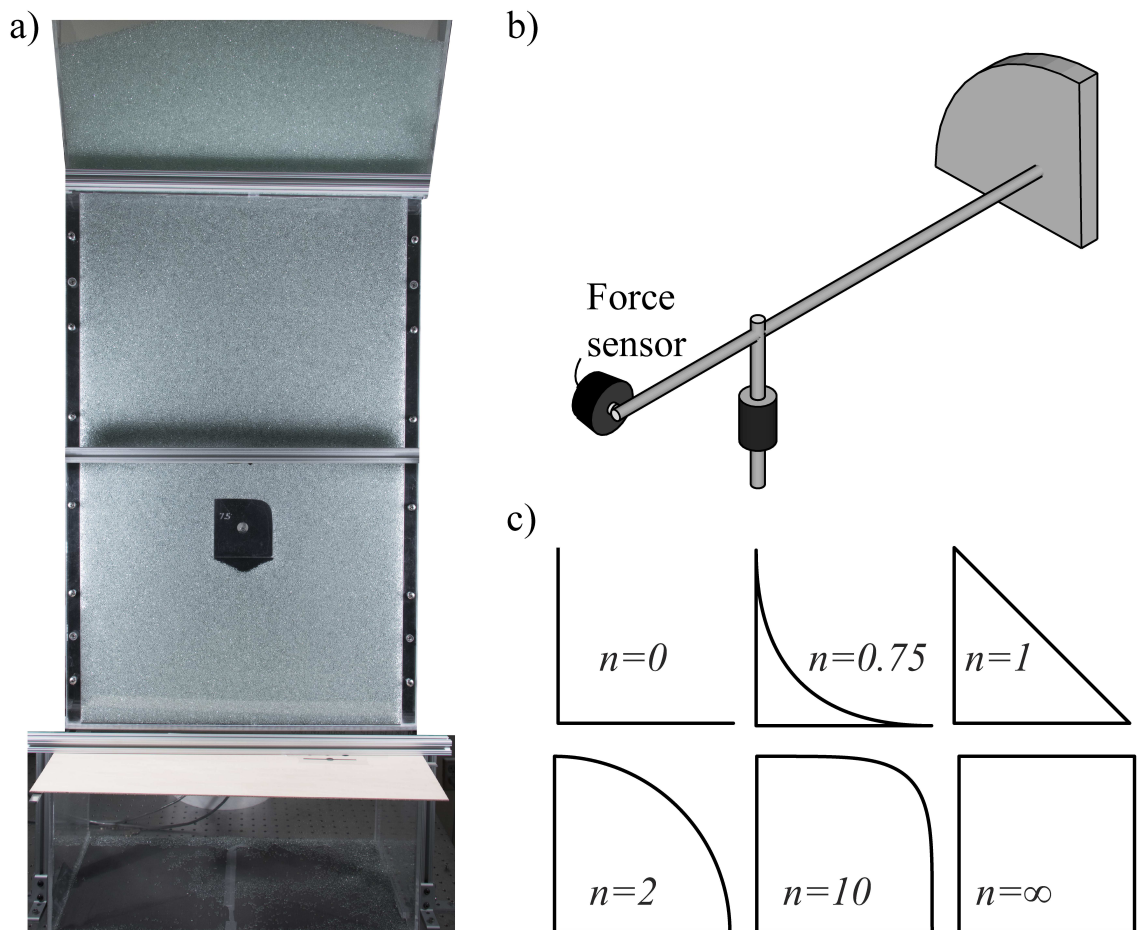


FIGURE 5. a) Front view of experimental setup. The intruder in the picture corresponds to a super-disk exponent  $n = 7.5$ . b) Intruder-sensor system schematic. c) Examples of intruders with different super-disk exponents. As  $n$  increases the shapes become more convex with  $n = \infty$  being a square.

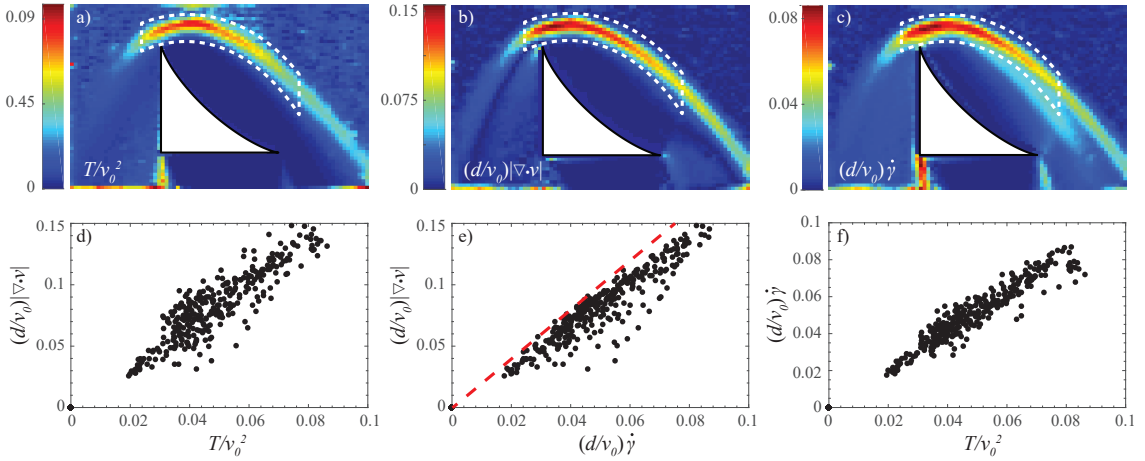


FIGURE 6. a-c) Intensity plot of scaled granular temperature, absolute divergence of the flow field, and local shear-strain rate for  $n = 0.75$ . d - f) Scatter plots of scaled flow-field divergence versus temperature, flow field divergence versus local shear rate, and shear rate versus temperature respectively, measured from all points enclosed by the white dotted regions.

We find that the asymmetry of the intruder alters the shock boundary and this in turn alters the lift force on the intruder. We propose a model for calculating lift forces which agrees with experimental data. We demonstrate that the force in the direction perpendicular to flow is the result of three mechanisms: 1) static loading from the dead zone above the intruder, 2) impact forces from the freely falling grains hitting the shock front, and 3) net momentum transfer due to mass ejection from the dead zone.

Our experimental setup consists of a rectangular quasi-2D granular hopper that is 1.25 cm deep, 55.8 cm wide, and 90 cm in height. The hopper is constructed from 1/4 inch acrylic as shown in Figure 5a. The front of the hopper is clear and the back is opaque to allow for quantitative imaging of the flow. The hopper is fed by a reservoir of 3 mm glass beads (Mo-Sci Corp) to provide a steady flow rate of approximately 400 particles  $\text{cm}^{-2}\text{s}^{-1}$ . A laser-cut acrylic intruder is placed inside the hopper and is constructed to be 1.1 cm thick, slightly thinner than the hopper cavity to prevent frictional contact with the front and back walls. The intruder is typically mounted at  $h=57$  cm below the reservoir, where the bead velocity in the absence of the intruder would be  $v_0=3.3$  m/s, comparable to the flow speeds in [39, 40, 43]. Changing  $h$  corresponds to changing the impact speed  $v_0$  of the grains;  $v_0 \propto \sqrt{h}$ .

Figure 5b shows the intruder-sensor system. The intruder is connected to one end of a 30 cm aluminum rod. The other end of the rod is held in place by a force sensor to measure

lateral forces (Measurement Specialties FC22) and a pre-load which is subtracted from the measurements. This rod is fixed to a second rod to form a T-shaped structure which is held by low friction bearings.

The intruder shape is defined as the first quadrant of the superdisk equation [44]

$$y = (1 - x^n)^{\frac{1}{n}}, \quad (3.1)$$

where  $x$  and  $y$  are the horizontal and vertical coordinates. The exponent  $n$  controls the concavity/symmetry of the shape as illustrated by the six shapes in Figure 5c. The superdisk equation provides a family of shapes interpolating from the asymmetric “L” at  $n = 0$  to a triangle at  $n = 1$ , a quarter circle at  $n = 2$  and a square at  $n = \infty$ . Unless otherwise specified the length  $R$  of the straight edge is held constant at 4 inches.

At the beginning of each measurement the bottom of the hopper is blocked off and it is filled with beads. When the beads are released the force sensor and a high-speed camera (Phantom M310) start recording. We ignore the initial transient (approximately 0-4 seconds) when beads begin to flow and keep only the measurements taken in steady state - when the flow rate is roughly constant. After about 10 seconds the reservoir is depleted.

For each value  $n$  we measure lateral forces on and granular flow field around the intruder. Bead velocities are calculated using particle image velocimetry [45]. In agreement with previous studies [41, 46–50] in steady state flow we observe a nearly stationary, densely packed pile of beads with a shock front above the leading edge of the intruder. The shock front can be identified by three different metrics - the local maxima of granular temperature  $T$ , flow divergence  $f_d$ , and shear strain rate  $\dot{\gamma}$ :

$$T = \langle \vec{v} \cdot \vec{v} \rangle - \langle \vec{v} \rangle \cdot \langle \vec{v} \rangle, \quad (3.2)$$

$$f_d = |\nabla \cdot \vec{v}|, \text{ and} \quad (3.3)$$

$$\dot{\gamma} = (d_1 - d_2)/2, \quad (3.4)$$

where  $\vec{v}$  is the velocity at any given point. Angled brackets denote time averages and  $d_1$  and  $d_2$  are eigenvalues of the strain rate tensor  $\mathbf{D} = \nabla \vec{v} + (\nabla \vec{v})^T$ , following the method described by Clark *et al.* [43].

## Results and Discussion

For all values of  $n$ , these three tests pick out the same feature above the intruder. They are shown for a representative intruder with  $n = 0.75$  in Figure 6a-c. These quantities are all close to zero everywhere else in the flow field. By picking out only the points inside the same dotted regions in Figures 6a-c, we plot divergence versus temperature, divergence versus shear rate and shear rate versus temperature in Figures 6d-f respectively. We non-dimensionalize these quantities by scaling them as  $T/v_0^2$ ,  $(d/v_0)|\nabla \cdot \vec{v}|$ , and  $(d/v_0)\dot{\gamma}$ , where  $v_0$  is the theoretical free-fall speed of the bead at the intruder's center of mass and  $d$  is the bead diameter. The linear relationship in each case shows that close to the shock boundary these three measurements are well correlated. In Figure 6e the red dotted line corresponds to a slope of 2. Since  $|f_d| = |d_1 + d_2|$  and  $\dot{\gamma} = d_1 - d_2$  where  $d_1$  and  $d_2$  are eigenvalues of the shear strain tensor, 6e shows that  $|d_1 + d_2| > \frac{1}{2}(d_1 - d_2)$ . The points in the scatter plot fall below the slope = 2 line (red dotted line in Figure 6e) showing that  $d_1 \gg d_2$ .

Figure 7a shows the extracted shock front for intruders of varying  $n$ . The plots show that the shock front maintains the same functional form as the intruder geometry is varied, with the curves shifting right and increasing in peak height with increasing  $n$ .

We model the shape of the shock front with simple force balance arguments similar to those of Mounfield and Edwards for a different problem; predicting the force along the arch in a jammed pipe [51]. In our system, during steady-state flow the shock front must remain stable. Any vertical or horizontal net force will result in a time variant shock front. To enforce stability of the arch-like shock front given the constraints of gravity the net force  $\vec{F}(s, \theta)$  must be always tangential to the surface of the shock as illustrated by the green arrow in Figure 8a (inset). This net force ensures that particles not absorbed by the quasi-static pile are cleared away from it such that the shock front remains stable. The ejection of particles from the left and right, illustrated by purple arrows in Figure 8a (inset), also ensure a stable shock position during steady flow.

The force  $\vec{F}(s, \theta)$  is expressed as a function of the arc length  $s$  and the angle of inclination with respect to the horizontal  $\theta$ . Furthermore, to sustain the arch-like shape there must be a tension  $F_T$  along it such that the horizontal and vertical components of the force at any point along it are given by  $F_x = F_T \cos \theta$  and  $F_y = F_T \sin \theta$  respectively. Following the steps outlined by

Mounfield and Edwards [51] we can describe the shock front by the euquation

$$y = w \cosh\left(\frac{x - c}{w}\right) + p. \quad (3.5)$$

Equation 3.5 is an inverted catenary where  $|w|$  is the characteristic width of the hyperbolic cosine curve,  $c$  sets the center of the curve, and  $p$  is the vertical offset such that  $y(x = c) = w + p$ . The measured shock fronts are well fit by this function as demonstrated by the dark lines on Figure 7a. Thus we find that in steady granular flow the shock front (ignoring temporal fluctuations) is a dynamic arch. By scaling out the fit parameters we find excellent collapse onto a single master curve, as demonstrated in figure 7b. This indicates that the influence of the intruder shape is limited to changing the centerpoint and height of the resulting shock wave.

To test the effect of intruder size,  $R$ , for a super-disk exponent  $n = 2$  we measured several combinations of varying  $R$  and height  $h$ . Figure 7b includes measurements for all probed values of  $n$  and all tested combinations  $(R, h)$  for  $n = 2$ . This provides strong evidence for the universality of the shape of the shock front; varying any of the parameters, intruder shape  $n$ , intruder size  $R$  and impact or incident grain velocity  $v_0$ , does not change the shape of the shock front. Finally, we created an intruder with no obvious symmetry (shown in Figure 2 of the Supplement) and found that its shock front, plotted as diamonds in Figure 7b, also collapses to the same master curve.

We obtain the constants  $w$ ,  $c$  and  $p$  as fit parameters to Equation 3.5 and plot them as functions of  $n$  in Figure 7c, where red circles represent data for varying  $n$  and blue squares represent data for different combinations  $(R, h)$  for  $n = 2$ . The plot of width  $w$  versus  $n$  demonstrates that the scaled width of the catenary is independent of the shape parameter  $n$  and the dotted line denotes the mean value  $-0.8$  of the curve width. The plot of center  $c$  versus  $n$  agrees with the qualitative observation from Figure 7a - the peaks shift away from the vertical edge as  $n$  goes from  $0 \rightarrow \infty$ . The center naturally asymptotes to  $c = 0.5$  for  $n \rightarrow \infty$  as the shape of the intruder approaches a symmetric square. We find that  $c$  roughly tracks the intruder center of mass (black solid curve). Plotting  $y(x = c)$ , which is the peak height  $w + p$ , as a function of  $n$  demonstrates that the peaks shift upwards with increasing  $n$ . Thus, we find that the intruder shape parameter  $n$  controls the catenary center and peak.

The shape of the catenary affects how grains are distributed on the intruder and thus, in turn, determines the lift forces  $F_L$ . We show this by directly measuring  $F_L$ , the lift force

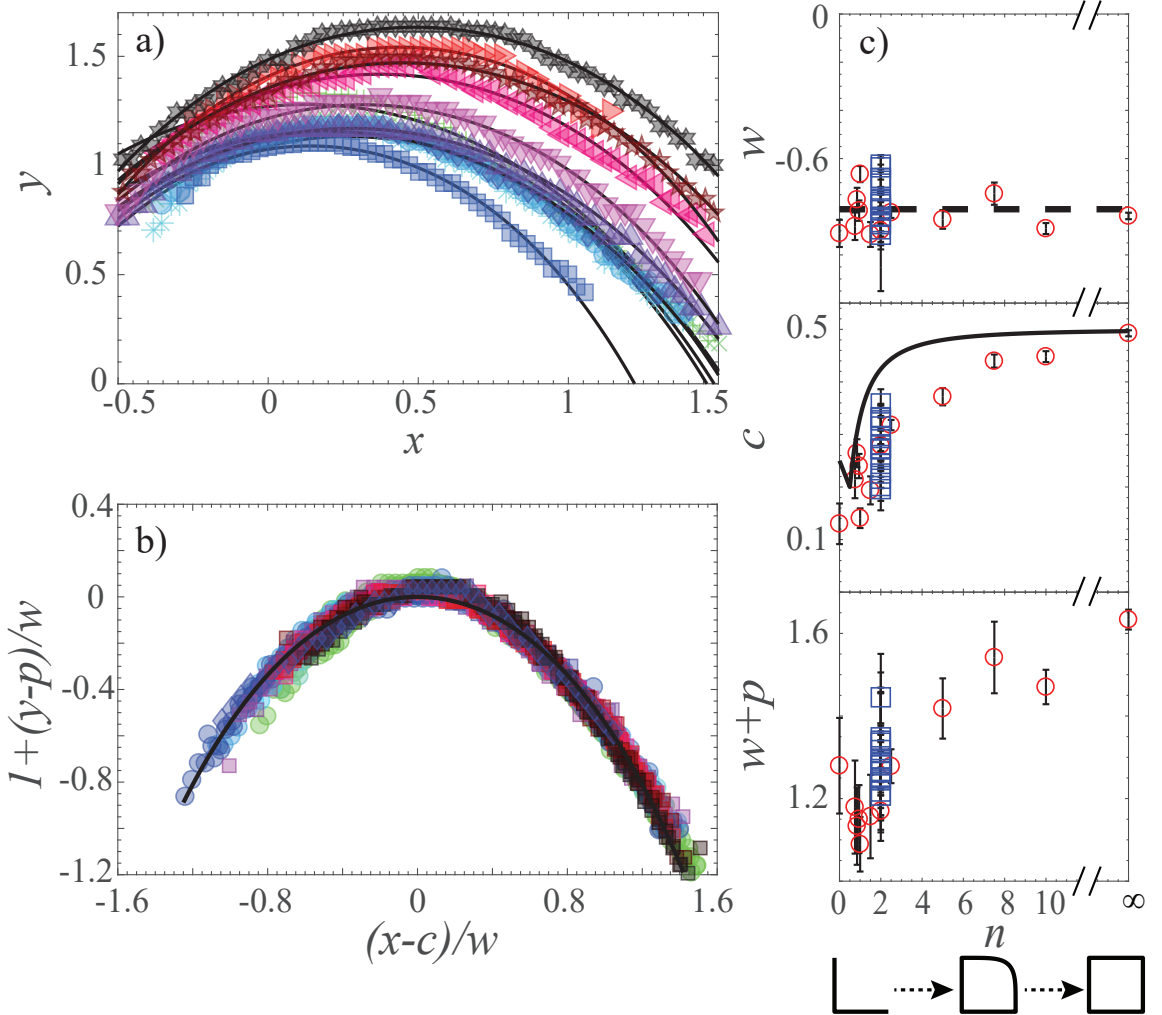


FIGURE 7. a) Plots of shock fronts. Scaled  $x$  and  $y$  coordinates are in units of  $R$ , the vertical length of the intruder. The data is shown for  $n = 0, 0.75, 0.85, 0.95, 1, 1.5, 2, 2.5, 5, 7.5, 10, \infty$ . Solid black lines are fits to Equation 3.5. b) Plot of scaled shock boundaries for all probed values of  $n$  with constant  $R = 4$  inches shown in circles. Squares represent all tested intruder locations  $h \in \{23, 34, 46, 57, 69, 84\}$  cm and intruder radii,  $R \in \{2, 3, 4, 7\}$  inches for constant  $n = 2$ . Diamond symbols represent data from an asymmetric intruder with random features on it (shown in Figure 2 of the Supplement). The black curve is the inverted catenary given by Equation 3.5. c) Top to bottom - plots of the fit parameters  $w$ ,  $c$  and  $w + p$  as functions of  $n$  respectively. Red circles represent data from varying  $n$  with constant  $R$  and blue squares represent data from fixed  $n = 2$  but different combinations of  $R$  and impact speed  $v_0$ . The dashed line shows the mean width  $|\bar{w}| \approx 0.8$ . In the  $c$  versus  $n$  plot the dark solid curve shows center of mass of the intruders shifts with varying  $n$ .

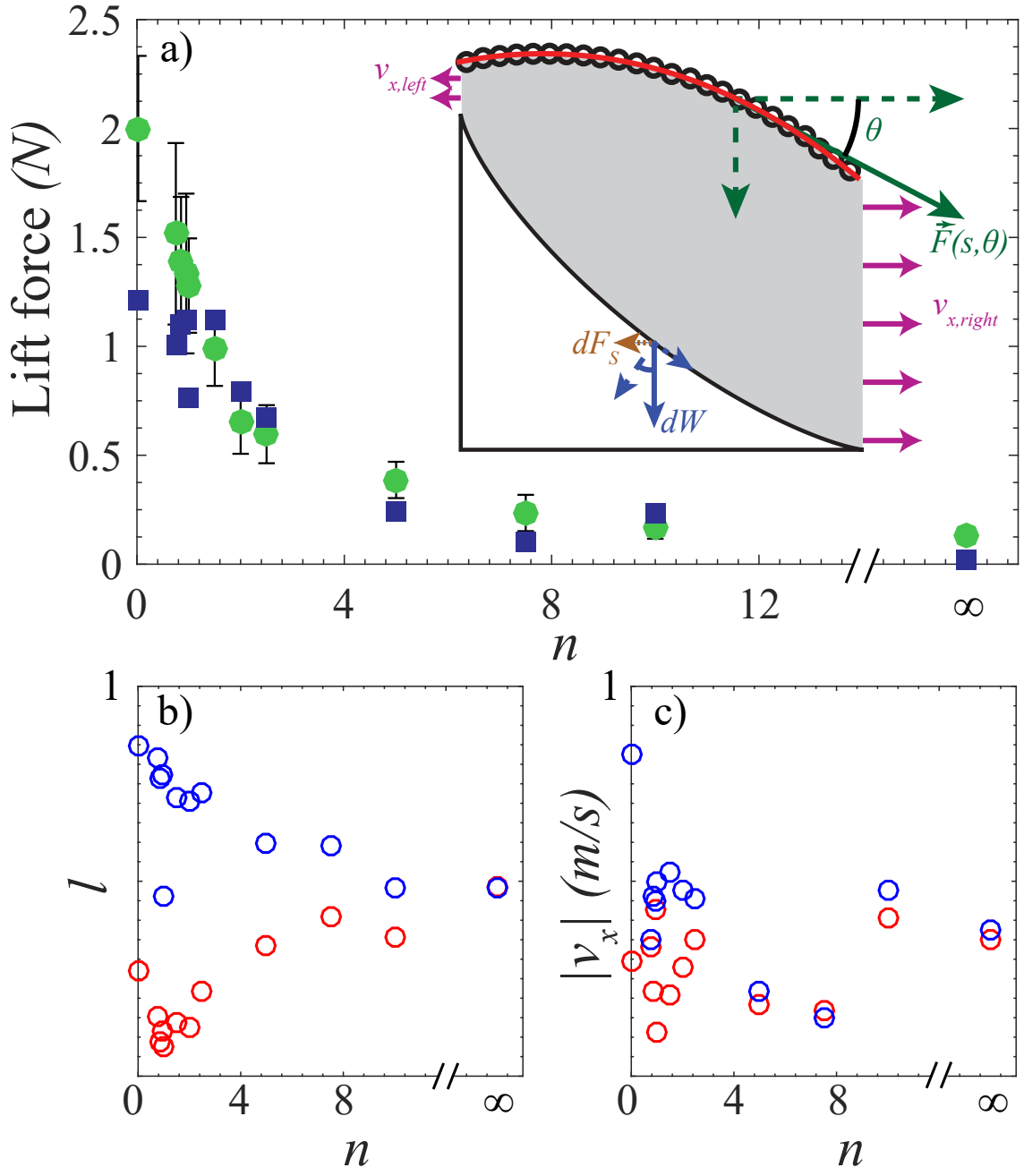


FIGURE 8. a) Plot of horizontal lift forces from force sensor (green circle) and calculated lift forces (dark blue squares) as a function of  $n$ . Lift is maximum for  $n \rightarrow 0$  and decreases to 0 as  $n \rightarrow \infty$ . Inset is an illustration showing the intruder, outlined in black, trapped grains, in grey and shock profile in red. The solid green arrow represents the tangential net force  $\vec{F}(s, \theta)$  on a small segment of the shock front. Dotted green arrows are components of this vector. Purple arrows labeled  $v_{x,0/1}$  represent horizontal ejected grain velocities from the trapped region. b) Plot of the left (red) and right (blue) exit heights  $l$  as a function of  $n$ . c) Plot of absolute horizontal left (red) and right (blue) exit velocities  $|v_x|$  versus  $n$ .

perpendicular to the direction of flow, on the intruder. The measured lift as a function of  $n$  is plotted as green circles in Figure 8a. The lift is maximum for  $n = 0$ , and decreases with increasing  $n$  and asymptotes to 0 as  $n \rightarrow \infty$ , in which case the intruder is perfectly symmetric. As detailed in the supplement we can model this lift force by considering three contributions: 1) the static load from the quasi-static pile, 2) the momentum flux from freely falling particles hitting the shock front and 3) momentum transfer from particles ejected from either side of the quasi-static pile.

The first contribution is from the horizontal component  $dF_S$  of the static load  $W$  pushing on the curved upper surface of the intruder. For all intruder shapes there is a trapped pile whose upper boundary is the shock front, which we can approximate as a static load. Because this load is resting on a curved, asymmetric surface it will impart a non-zero horizontal component  $F_S$ , which is calculated explicitly in the supplement. In the limiting cases  $n = 0$  or  $\infty$  this contribution goes to zero.

The second force contribution is from the momentum flux of freely falling particles impacting the shock front. This force,  $F_C$  is equal to the incident mass per unit time perpendicular to the shock front multiplied by the velocity change in the horizontal direction. The incident velocities along the shock front are taken from PIV measurements, a representative plot of which is shown for  $n = 0.75$  in Figure 4 of the Supplement.

The third force contribution  $F_{flow}$  is from grains being ejected from the area between the shock front and the intruder profile. These grains are measured to leave with average speeds  $v_{x,left}$  and  $v_{x,right}$  illustrated by purple arrows in Figure 8a inset. Since we keep the width of the hopper constant the scaled heights  $l_{left}$  and  $l_{right}$ , distances from the intruder to the shock front at  $x = 0$  (red circles) and  $x = 1$  (blue circles) respectively, are measures of the exit areas. The distances  $l_{left/right}$  are plotted as functions of  $n$  in Figure 8b. The distances are scaled by the intruder size  $R$  as before. We find that the difference in the two exit areas ( $|l_{left} - l_{right}|$ ) decreases with increasing  $n$  and becomes equal at  $n = \infty$ . This implies that for equal exit velocities more grains can escape from the exit area at  $x = 1$ , which in turn means greater momentum flux at this edge.

The mean exit velocities at  $x = 0$  (red circles) and  $x = 1$  (blue circles) obtained from PIV measurements are plotted in Figure 8c and we find that the speeds are roughly the same

and nearly equal for  $n > 2$ . Thus, for asymmetrical intruders the disparity in granular exit areas becomes the dominating factor. At smaller  $n$ , as the shape becomes more concave and asymmetric, the momentum flux on the right at  $x = 1$  is greater so  $F_{flow}$  is higher. For larger values of  $n$  the two areas and speeds are comparable so net momentum flux,  $F_{flow}$  approaches zero for  $n \rightarrow \infty$ .

Our results reveal that in the region near the granular shock front the mean flow field variance, absolute flow field divergence and shear strain rate are linearly related to each other. The local maxima in each of these measurements provide a robust means of identifying the shock front. The shock front is characterized by a universal functional form that is, unlike the fluid flow analog, invariant with respect to intruder size, shape and impact speeds within probed experimental values. To enforce stability given the constraints of gravity and granular impact forces there must always be a tangential force along the shock front. This leads to an appropriate organization of quasi-static grains around the intruder such that the effective shape becomes arch-like and well described by an inverted catenary. The catenary center lines ( $x = c$ ) roughly track the intruders' centers of mass ( $x = x_m$ ). The two lines begin to converge as the intruder approaches a more symmetrical shape. Variation in intruder geometry results in scaling and shifting of the catenary and this determines the lift force on the intruder. We also demonstrate that the mechanism for lift in dilute granular flows consists of at least three processes rather than just collisional forces as might be naively expected.

In dilute flows, the quasi-static granular pack is analogous to a hydrodynamic radius and determines the effective shape of an intruding object. The existence of several metrics to identify the shock boundary and universality in its shape should pave the way for a better understanding of boundary conditions and more refined applications of Navier-Stokes-like continuum models to dilute granular flows. Our work also presents avenues for future exploration of drag forces on intruder shape, size and impact speeds. This future work would further detail the extent to which granular lift is drag-induced.

## CHAPTER IV

### SUPPLEMENTARY MATERIALS FOR CHAPTER III

#### Forces on Grain Pile

The lift force  $F_L$  can be described by a simple model consisting of three parts: the horizontal component of the static load  $F_S$ , the horizontal component of the impact forces  $F_C$ , and the horizontal forces due to momentum transfer of outflowing particles  $F_{flow}$ .

The static pile above the intruder has a mass proportional to the volume enclosed by the shock front and the intruder profile, shown by the grey region in Figure 9. For a given exponent  $n$ , the shape of the intruder profile is given by  $g(x) = (1 - x^n)^{1/n}$  and the shock front  $f(x)$  given by Equation 5 in the main article. For a small segment of the trapped area of width  $dx$  and thickness  $w_{cell}$  the volume  $dV = w_{cell}[f(x) - g(x)]dx$ . The net horizontal component of this weight is given by

$$F_S = \int_0^1 w_{cell}[f(x) - g(x)]\phi\rho_g g \cos(\alpha(x)) \sin(\alpha(x)) dx \quad (4.1)$$

where the density of glass is  $\rho_g = 2500 \text{ kg/m}^3$ ,  $g$  is gravitational acceleration and  $\alpha(x)$  the angle between the horizontal and tangent to  $g(x)$ . This contribution is shown on Figure 11 as the downward pointing triangles. We approximate the volume fraction  $\phi = 0.6$ , slightly lower than random close packing because of the presence of confining walls in our system which is about 8 bead diameters thick. The cosine term gives the normal component to the tangent and the sine resolves the horizontal component. The horizontal component of the force is integrated over the length of the intruder to calculate the lift force due to the static pack. The integration limits are  $x \in [0, 1]$  where  $x = 0$  and  $x = 1$  are the left and right edges of the intruder respectively.

The collisional force  $F_C$  (upward pointing triangles on Figure 11) due to beads impacting the shock boundary and is given by

$$F_C = \int_0^1 \phi_d \rho_g w_{cell} [\vec{v}(x) \cdot \hat{n}(x)]^2 \sin \theta(x) dx \quad (4.2)$$

where  $\phi_d \rho_g w_{cell} \vec{v}(x) \cdot \hat{n}(x) dx$  is the incident mass per unit time at  $x$  on a small segment  $dx$  of the shock front.  $\theta(x)$  is the angle between the horizontal and tangent to  $f(x)$ . The normal component of the incident velocity of particles colliding with the shock front is given by

$\vec{v}(x) \cdot \hat{n}(x)$ . The velocities are obtained from PIV measurements of the flow field, as shown by a representative image of the field overlaid on the intruder in Figure 12. The fraction of space occupied by freely falling particles is  $\phi_d \approx 0.03$  as measured directly from the images. Assuming that collisions are inelastic, the rate of momentum transfer normal to  $f(x)$  is  $\phi_d \rho_g w_{cell} (\vec{v}(x) \cdot \hat{n}(x) dx) (\vec{v}(x) \cdot \hat{n}(x)) \sin \theta(x)$ . The sine term comes from the horizontal component of this force at  $g(x)$ .

The horizontal reaction force  $F_{flow}$  (represented by diamonds on Figure 11) on the intruder due to mass ejection from the granular pile is

$$F_{flow} = \phi \rho w_{cell} ([f(1) - g(1)] v_{x,1}^2 - [f(0) - g(0)] v_{x,0}^2) \quad (4.3)$$

where  $\phi \rho w_{cell} ([f(x_0) - g(x_0)] v^2)$  is the horizontal momentum transferred due to particles being ejected from the area between  $f(x_0)$  and  $g(x_0)$ . The velocities  $v_{x,0}$  and  $v_{x,1}$  are the mean horizontal bead velocities exiting the cross-section  $w_{cell}[f(x) - g(x)]$  at  $x = 0$  and  $x = 1$  respectively. The volume fraction is  $\phi = 0.6$ .

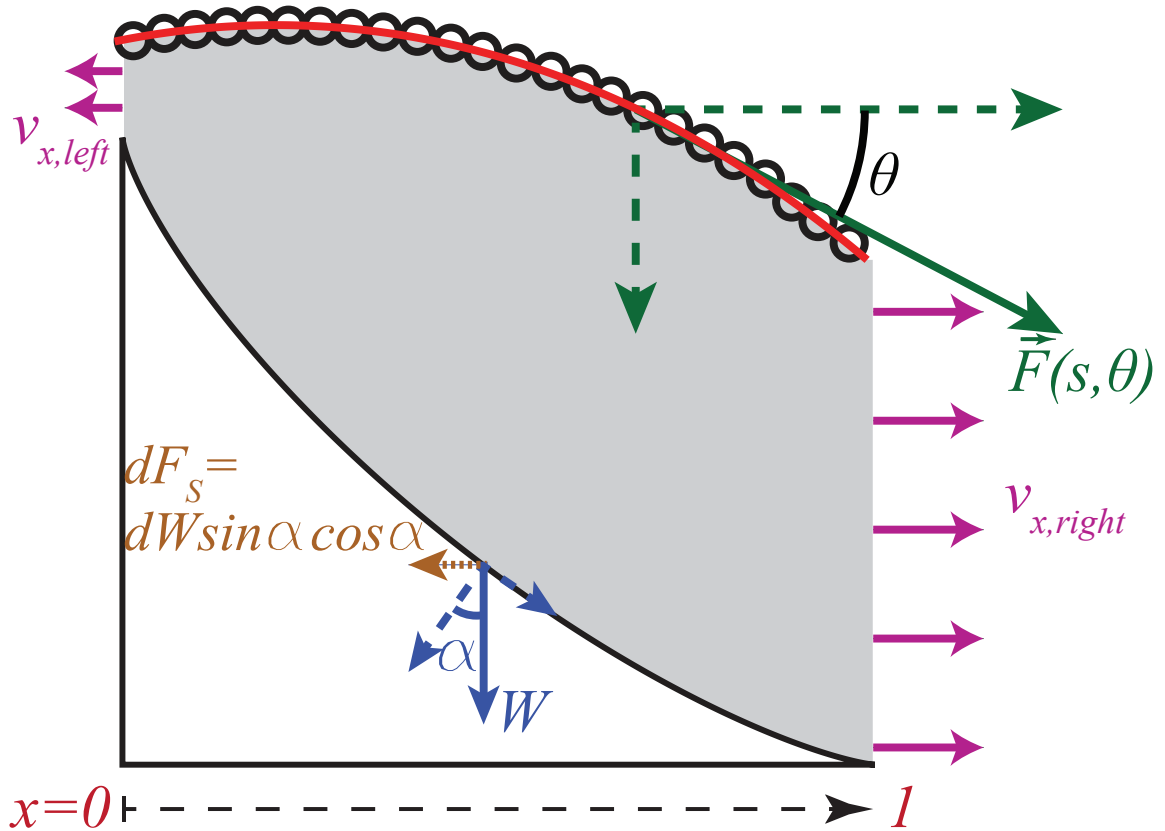


FIGURE 9. Diagram of force vectors and velocities used to calculated  $F_L$ .

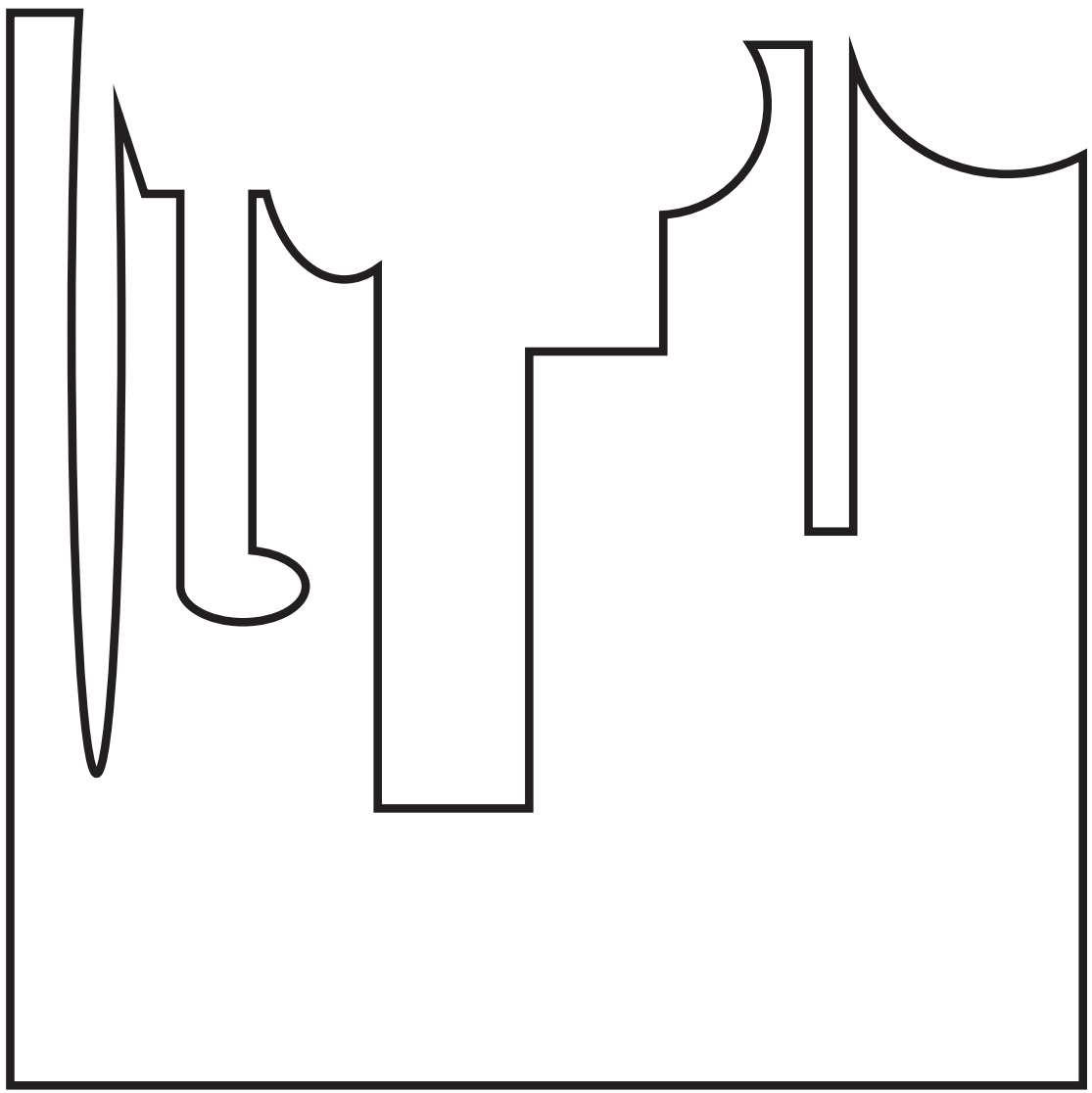


FIGURE 10. Illustration of the intruder with random features on the leading edge. The shock front from this shape still maintains the catenary shape.

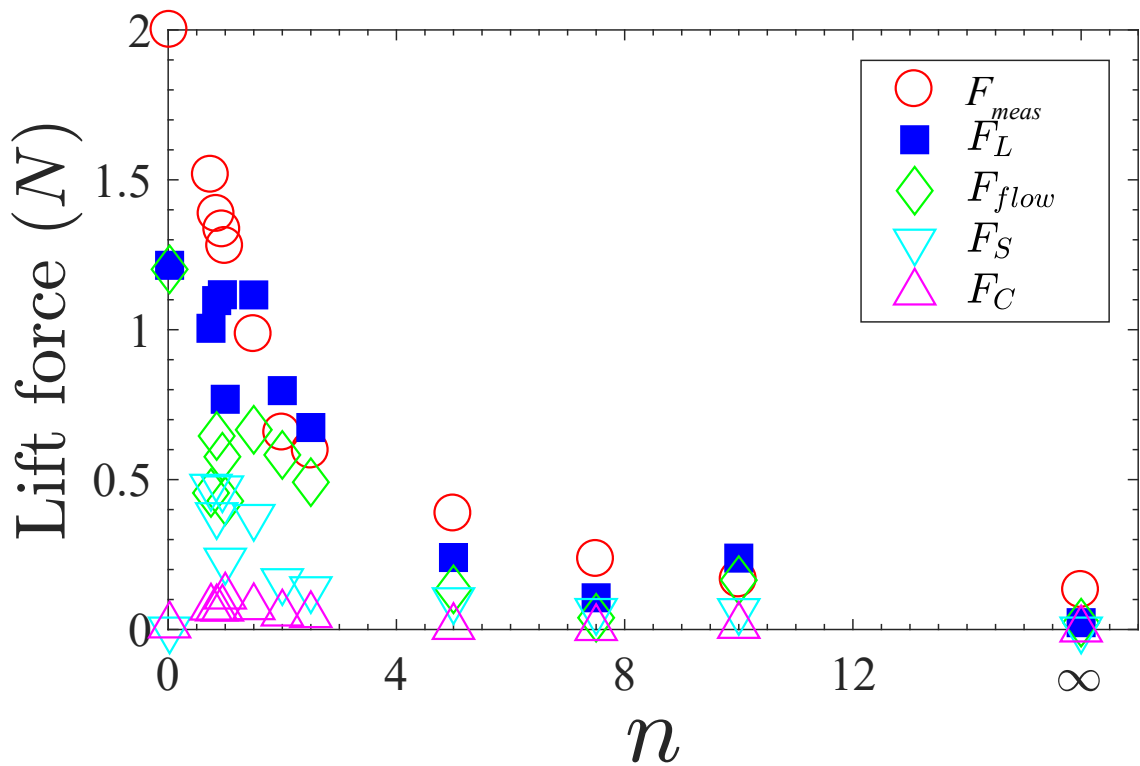


FIGURE 11. Plots of total measured lift force  $F_{meas}$ , calculated lift force  $F_L$  (blue squares), force due to mass ejection from trapped pile  $F_{flow}$  (green diamond), quasi-static load contribution  $F_S$  (downward pointing arrow), and force due to impacts  $F_C$  (upward pointing arrow) as a function of  $n$ .

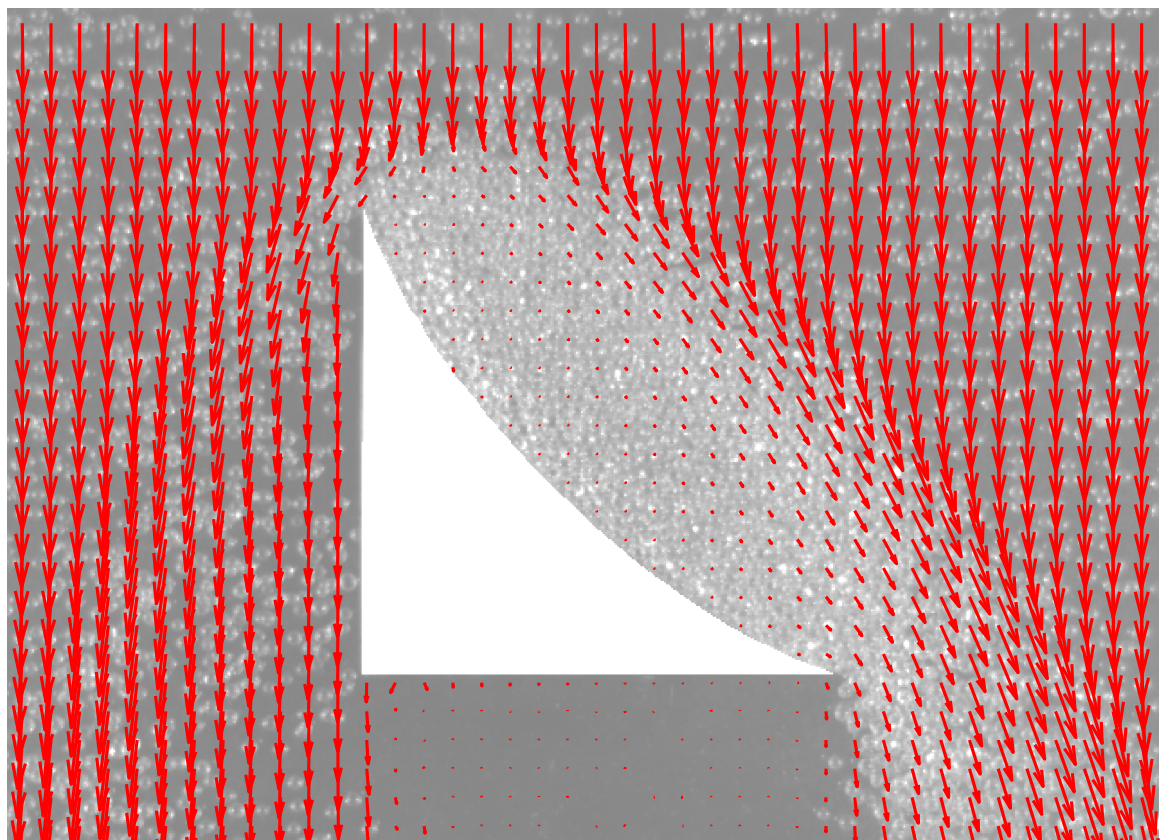


FIGURE 12. Representative mean flow field around an intruder with super-disk exponent  $n = 0.75$ . The white masked out region is the intruder and the arrows are velocity vectors.

## CHAPTER V

### CONCLUSION

The unifying theme of this work is the physics of granular materials, both stationary and in a state of flow. We have further illustrated the ability of granular materials to exhibit solid-like and liquid-like behavior. We have detailed methods of tuning external conditions to preferentially retain one quality or the other.

Chapter II focused on a well-known property of static granular systems concerning the pressure at the bottom of a container with grains. More than a hundred years ago, the Janssen equation described the property of contained granular systems to redirect increased load to the side walls. This means there is a saturation of pressure at the container base but an increase in load on side walls. In this work we demonstrated conditions necessary to sustain this phenomena. We also demonstrated how to tune the geometry of the system to recover the original Janssen effect.

In contrast to Janssen's original experiment we constructed a two-dimensional granular system laid out horizontally, compacted by friction provided by a conveyor belt. We therefore removed the effect of gravity and could focus on the role of friction. We showed that with a constantly slipping surface and straight side-walls the system surprisingly behaves like a hydrostatic system following Stevin's law. In other words, Janssen's equation fails to capture the physics of the system.

This vanishing of the Janssen effect is due to the slipping surface weakening frictional contacts between the grains and the side-walls. To recover the Janssen effect, we redesigned the side walls to consist of sawtooth patterns. The edges of the sawtooth were the same length scale as the grains to ensure enduring contacts. With the sawtooth walls there is a constant mechanical reaction force that replaces friction in a system with straight side walls. We found that even with the slipping surface of the conveyor belt this mechanical force is sufficient to enforce necessary conditions to redirect load to the side walls. Furthermore, this mechanical force can be tuned by the sawtooth angle and this determines the rate at which the bottom pressure saturates. This study illustrates the importance of friction in granular systems; the presence (or absence) of friction sets the onset of fluid-like properties.

Chapter III focused on a different aspect of granular materials specifically the characterization of shock fronts and consequent lift forces on obstructed granular flows. A quasi-two-dimensional hopper was constructed to provide steady dilute flow. The obstacle profile was derived from a family of curves known as super-disks. This enabled us to control its shape by tuning a single parameter the exponent of the super-disk. We observed flows for several values of this exponent for a fixed obstacle size and granular impact speed.

For all shape exponents the flow resulted in the formation of a quasi-static pile on the obstacle with a shock front separating this and the free flowing beads. We calculated flow fields by applying particle image velocimetry (PIV) and measured the lift force from a force sensor connected to the obstacle. To characterize the shock front and its effect on the flow field, we calculated the granular temperature (defined as the variance of the flow field), the flow field divergence and the shear-strain. Surprisingly we found a strong linear correlation between all three quantities near the shock front.

We characterized the shock front as the local maxima of each measurement and showed that it is very well described by an inverted catenary. We derive the inverted catenary shape by applying simple force balance arguments and proper constraints. We find that unlike obstructed fluid flows, granular shock fronts maintain the same functional form across varying obstacle shapes and sizes and even impact speeds. This invariance in shock profile with respect to obstacle geometry is due to the quasi-static grains piling up to present the same shape.

The functional form of the shock profile allows for accurate calculation of the lift force on the intruder. By calculating the force contributions from impact on the shock front as defined by catenary, momentum flux from quasi-static pile and horizontal component of the quasi-static load we can calculate the net lift on the obstacle. The agreement of the force calculation with direct force measurements is further evidence that the catenary description of the shock front is appropriate.

This system constructed for studying granular flows has several avenues for further inquiry. In the current study the flow rate was kept constant for all measurements. It would be interesting to study the formation of the quasi-static pile by varying the flow rate. At very low flow rates the quasi-static pile would not exist. At what flow rate does this granular pile start to form? And what determines this value? The bead reservoir at the top of the experimental system can be

modified slightly to achieve different flow rates. For instance the opening through the reservoir can be constricted to gradually lower the flow rate. Studying the relationship between the flow rate and the dimensions of the system (system, intruder and particle sizes) would be an easy next step to study the factors determining the formation of the quasi-static grain piles.

The system can also be easily modified very easily to study drag and torque on the obstacle. Measuring drag would be easier. This would involve simply rotating the hinged mount holding the rod connected to the intruder. Measuring drag would be further verification for the force model we have employed to describe the lift on the shapes. Measuring torque is slightly more complicated. This would involve building intruders with bearings that allow them to rotate. The rotational motion can be measured using an optical encoder or image analysis. These measurements may shed light on whether, for instance, the quasi-static granular pile is minimizing the net torque on the obstacle.

Another important topic of further research is the relationship between granular temperature, flow divergence and shear strain rate near the shock front. We observe that these measurements are linearly related but do not have a strong grasp of the reason behind this. One option to delve into the matter would be to pick a shape and size for an intruder and perform PIV calculations at very high resolutions to parse the behavior of beads at different regions in the shock front and quasi-static pile. The motion of the beads inside the quasi-static pile likely plays a role in determining the shock front and the forces on the intruder.

The experiments described above further illustrate how granular systems are replete with interesting phenomena that we do not fully understand. We know a little more when Janssen's equation fails and grains start to behave like liquids; and we know how to exploit geometry to retrieve Janssen's effect in the same system. We also show the tendency of obstructed grain flows to organize into predictably shaped piles that are surprisingly independent of obstacle shape, size and impact speed. While this work was driven by curiosity the results will hopefully extend our ability to predict the nature of granular matter that we find all around us.

## REFERENCES CITED

- [1] Peter Schiffer. Granular physics: A bridge to sandpile stability. *Nature Physics*, 1(1):21–22, October 2005. ISSN 1745-2473. doi: 10.1038/nphys129. URL <http://www.nature.com/nphys/journal/v1/n1/full/nphys129.html>.
- [2] R. Allen Wilkinson, Robert P. Behringer, James T. Jenkins, and Michel Y. Louge. Granular materials and the risks they pose for success on the moon and mars. *AIP Conference Proceedings*, 746(1):1216–1223, 2005. doi: 10.1063/1.1867248. URL <http://aip.scitation.org/doi/abs/10.1063/1.1867248>.
- [3] Nikolai Brilliantov, P. L. Krapivsky, Anna Bodrova, Frank Spahn, Hisao Hayakawa, Vladimir Stadnichuk, and Jrgen Schmidt. Size distribution of particles in Saturns rings from aggregation and fragmentation. *Proceedings of the National Academy of Sciences*, 112(31):9536–9541, August 2015. ISSN 0027-8424, 1091-6490. doi: 10.1073/pnas.1503957112. URL <http://www.pnas.org/content/112/31/9536>.
- [4] Ronald-Louis Ballouz, Derek C. Richardson, and Ryuji Morishima. Numerical simulations of saturns b ring: Granular friction as a mediator between self-gravity wakes and viscous overstability. *The Astronomical Journal*, 153(4):146, 2017. URL <http://stacks.iop.org/1538-3881/153/i=4/a=146>.
- [5] Jacques Duran. *Sands, powders, and grains: an introduction to the physics of granular materials*. Springer, New York, 2000. ISBN 0387986561 9780387986562.
- [6] Heinrich M. Jaeger, Sidney R. Nagel, and Robert P. Behringer. Granular solids, liquids, and gases. *Reviews of Modern Physics*, 68(4):1259–1273, October 1996. doi: 10.1103/RevModPhys.68.1259. URL <http://link.aps.org/doi/10.1103/RevModPhys.68.1259>.
- [7] Anthony Rosato, Katherine J. Strandburg, Friedrich Prinz, and Robert H. Swendsen. Why the brazil nuts are on top: Size segregation of particulate matter by shaking. *Phys. Rev. Lett.*, 58:1038–1040, Mar 1987. doi: 10.1103/PhysRevLett.58.1038. URL <https://link.aps.org/doi/10.1103/PhysRevLett.58.1038>.
- [8] Daniel C. Hong, Paul V. Quinn, and Stefan Luding. Reverse brazil nut problem: Competition between percolation and condensation. *Phys. Rev. Lett.*, 86:3423–3426, Apr 2001. doi: 10.1103/PhysRevLett.86.3423. URL <https://link.aps.org/doi/10.1103/PhysRevLett.86.3423>.
- [9] H. A. Janssen. Versuche über getreidedrack in silozellen. *Zeitschrift des Vereines Deutscher Ingenieure*, 39:1045–1049, 1895. URL <http://www.phy.duke.edu/~msperl/Janssen/Janssen1895.pdf>.
- [10] M. Yasinul Karim and Eric I. Corwin. Eliminating friction with friction: 2d janssen effect in a friction-driven system. *Phys. Rev. Lett.*, 112:188001, May 2014. doi: 10.1103/PhysRevLett.112.188001. URL <https://link.aps.org/doi/10.1103/PhysRevLett.112.188001>.
- [11] Herbert Goldstein, Charles Poole, John Safko, and Stephen R. Addison. Classical Mechanics, 3rd ed. *American Journal of Physics*, 70(7):782–783, 2002. ISSN 0002-9505. doi: 10.1119/1.1484149.

- [12] A. Mareno and L. Q. English. The stability of the catenary shapes for a hanging cable of unspecified length. *European Journal of Physics*, 30(1):97, 2009. URL <http://stacks.iop.org/0143-0807/30/i=1/a=010>.
- [13] H. M. Jaeger and Sidney R. Nagel. Physics of the granular state. *Science*, 255(5051):1523–1531, March 1992. ISSN 0036-8075, 1095-9203. doi: 10.1126/science.255.5051.1523. URL <http://www.sciencemag.org/content/255/5051/1523>. PMID: 17820163.
- [14] Andrea J. Liu and Sidney R. Nagel. Nonlinear dynamics: Jamming is not just cool any more. *Nature*, 396(6706):21–22, November 1998. ISSN 0028-0836. doi: 10.1038/23819. URL <http://www.nature.com/nature/journal/v396/n6706/full/396021a0.html>.
- [15] V. Trappe, V. Prasad, Luca Cipelletti, P. N. Sege, and D. A. Weitz. Jamming phase diagram for attractive particles. *Nature*, 411(6839):772–775, June 2001. ISSN 0028-0836. doi: 10.1038/35081021. URL <http://www.nature.com/nature/journal/v411/n6839/full/411772a0.html>.
- [16] Matthias Sperl. Experiments on corn pressure in silo cells translation and comment of janssen’s paper from 1895. *Granular Matter*, 8(2):59–65, May 2006. ISSN 1434-5021, 1434-7636. doi: 10.1007/s10035-005-0224-z. URL <http://link.springer.com/article/10.1007/s10035-005-0224-z>.
- [17] R.M. Nedderman, U. Tüzün, S.B. Savage, and G.T. Houslby. The flow of granular materials: Discharge rates from hoppers. *Chemical Engineering Science*, 37(11):1597–1609, 1982. ISSN 0009-2509. doi: 10.1016/0009-2509(82)80029-8. URL <http://www.sciencedirect.com/science/article/pii/0009250982800298>.
- [18] Leo P. Kadanoff. Built upon sand: Theoretical ideas inspired by granular flows. *Reviews of Modern Physics*, 71(1):435–444, January 1999. doi: 10.1103/RevModPhys.71.435. URL <http://link.aps.org/doi/10.1103/RevModPhys.71.435>.
- [19] P. G. de Gennes. Granular matter: a tentative view. *Reviews of Modern Physics*, 71(2):S374–S382, March 1999. doi: 10.1103/RevModPhys.71.S374. URL <http://link.aps.org/doi/10.1103/RevModPhys.71.S374>.
- [20] Yann Bertho, Frédérique Giorgiutti-Dauphiné, and Jean-Pierre Hulin. Dynamical janssen effect on granular packing with moving walls. *Physical Review Letters*, 90(14), April 2003. ISSN 0031-9007, 1079-7114. doi: 10.1103/PhysRevLett.90.144301.
- [21] James W. Landry, Gary S. Grest, Leonardo E. Silbert, and Steven J. Plimpton. Confined granular packings: Structure, stress, and forces. *Physical Review E*, 67(4):041303, April 2003. doi: 10.1103/PhysRevE.67.041303. URL <http://link.aps.org/doi/10.1103/PhysRevE.67.041303>.
- [22] C. Mankoc, A. Janda, R. Arévalo, J. M. Pastor, I. Zuriguel, A. Garcimartín, and D. Maza. The flow rate of granular materials through an orifice. *Granular Matter*, 9(6):407–414, November 2007. ISSN 1434-5021, 1434-7636. doi: 10.1007/s10035-007-0062-2. URL <http://link.springer.com/article/10.1007/s10035-007-0062-2>.
- [23] J. E. Hilton and P. W. Cleary. Granular flow during hopper discharge. *Physical Review E*, 84(1):011307, July 2011. doi: 10.1103/PhysRevE.84.011307. URL <http://link.aps.org/doi/10.1103/PhysRevE.84.011307>.
- [24] M. A. Aguirre, J. G. Grande, A. Calvo, L. A. Pugnaloni, and J.-C. Géminard. Pressure independence of granular flow through an aperture. *Physical Review Letters*, 104(23):238002, June 2010. doi: 10.1103/PhysRevLett.104.238002. URL <http://link.aps.org/doi/10.1103/PhysRevLett.104.238002>.

- [25] María Alejandra Aguirre, Juan Gabriel Grande, Adriana Calvo, Luis A. Pugnaloni, and Jean-Christophe Géminard. Granular flow through an aperture: Pressure and flow rate are independent. *Physical Review E*, 83(6):061305, June 2011. doi: 10.1103/PhysRevE.83.061305. URL <http://link.aps.org/doi/10.1103/PhysRevE.83.061305>.
- [26] Zénó Farkas, Ferenc Szalai, Dietrich E. Wolf, and Tamás Vicsek. Segregation of granular binary mixtures by a ratchet mechanism. *Physical Review E*, 65(2):022301, January 2002. doi: 10.1103/PhysRevE.65.022301. URL <http://link.aps.org/doi/10.1103/PhysRevE.65.022301>.
- [27] Shahin Mobarakabadi, Ehsan Nedaaee Oskooe, Matthias Schröter, and Mehdi Habibi. Granular transport in a horizontally vibrated sawtooth channel. *Physical Review E*, 88(4):042201, October 2013. doi: 10.1103/PhysRevE.88.042201. URL <http://link.aps.org/doi/10.1103/PhysRevE.88.042201>.
- [28] I. Derényi, P. Tegzes, and T. Vicsek. Collective transport in locally asymmetric periodic structures. *Chaos: An Interdisciplinary Journal of Nonlinear Science*, 8(3):657, 1998. ISSN 10541500. doi: 10.1063/1.166348. URL <http://scitation.aip.org/content/aip/journal/chaos/8/3/10.1063/1.166348>.
- [29] Z. Farkas, P. Tegzes, A. Vukics, and T. Vicsek. Transitions in the horizontal transport of vertically vibrated granular layers. *Physical Review E*, 60(6):7022–7031, December 1999. doi: 10.1103/PhysRevE.60.7022. URL <http://link.aps.org/doi/10.1103/PhysRevE.60.7022>.
- [30] Robert Andrew Caughey, Calvin W. Tooles, and Alfred C. Scheer. *Lateral and vertical pressure of granular material in deep bins*. Iowa State College of Agriculture and Mechanic Arts, 1951.
- [31] V. Sundaram and S.C. Cowin. A reassessment of static bin pressure experiments. *Powder Technology*, 22(1):23–32, January 1979. ISSN 0032-5910. doi: 10.1016/0032-5910(79)85004-4. URL <http://www.sciencedirect.com/science/article/pii/0032591079850044>.
- [32] A.O. Atewologun and G.L. Riskowski. Experimental determination of janssen's stress ratio by four methods for soybeans under static conditions. *Transactions of the ASAE*, 34, 1991. ISSN 0001-2351.
- [33] R. Rusinek. Experimental method for determination of the pressure distribution in granular solids. *Research in Agricultural Engineering - UZPI*, v. 49(2) p., June 2003. ISSN 1212-9151.
- [34] Raenell Soller and Stephan A. Koehler. Drag and lift on rotating vanes in granular beds. *Phys. Rev. E*, 74(2):021305, August 2006. doi: 10.1103/PhysRevE.74.021305. URL <http://link.aps.org/doi/10.1103/PhysRevE.74.021305>.
- [35] Yang Ding, Nick Gravish, and Daniel I. Goldman. Drag induced lift in granular media. *Phys. Rev. Lett.*, 106(2):028001, January 2011. doi: 10.1103/PhysRevLett.106.028001. URL <http://link.aps.org/doi/10.1103/PhysRevLett.106.028001>.
- [36] Fabricio Q. Potiguar. Lift force on an asymmetrical obstacle immersed in a dilute granular flow. *Phys. Rev. E*, 84(6):061302, December 2011. doi: 10.1103/PhysRevE.84.061302. URL <http://link.aps.org/doi/10.1103/PhysRevE.84.061302>.

- [37] Fabricio Q. Potiguar and Yang Ding. Lift and drag in intruders moving through hydrostatic granular media at high speeds. *Phys. Rev. E*, 88(1):012204, July 2013. doi: 10.1103/PhysRevE.88.012204. URL <http://link.aps.org/doi/10.1103/PhysRevE.88.012204>.
- [38] P. K. Haff. Grain flow as a fluid-mechanical phenomenon. *Journal of Fluid Mechanics*, 134: 401–430, September 1983. ISSN 1469-7645, 0022-1120. doi: 10.1017/S0022112083003419.
- [39] Erin C. Rericha, Chris Bizon, Mark D. Shattuck, and Harry L. Swinney. Shocks in Supersonic Sand. *Phys. Rev. Lett.*, 88(1):014302, December 2001. doi: 10.1103/PhysRevLett.88.014302. URL <http://link.aps.org/doi/10.1103/PhysRevLett.88.014302>.
- [40] Yacine Amarouchene and Hamid Kellay. Speed of sound from shock fronts in granular flows. *Physics of Fluids (1994-present)*, 18(3):031707, March 2006. ISSN 1070-6631, 1089-7666. doi: 10.1063/1.2185689. URL <http://scitation.aip.org/content/aip/journal/pof2/18/3/10.1063/1.2185689>.
- [41] J. F. Boudet, Y. Amarouchene, and H. Kellay. Shock front width and structure in supersonic granular flows. *Phys. Rev. Lett.*, 101(25):254503, December 2008. doi: 10.1103/PhysRevLett.101.254503. URL <http://link.aps.org/doi/10.1103/PhysRevLett.101.254503>.
- [42] J. F. Boudet and H. Kellay. Drag coefficient for a circular obstacle in a quasi-two-dimensional dilute supersonic granular flow. *Phys. Rev. Lett.*, 105(10):104501, August 2010. doi: 10.1103/PhysRevLett.105.104501. URL <http://link.aps.org/doi/10.1103/PhysRevLett.105.104501>.
- [43] Abram H. Clark, Lou Kondic, and Robert P. Behringer. Steady flow dynamics during granular impact. *Phys. Rev. E*, 93(5):050901, May 2016. doi: 10.1103/PhysRevE.93.050901. URL <http://link.aps.org/doi/10.1103/PhysRevE.93.050901>.
- [44] Y. Jiao, F. H. Stillinger, and S. Torquato. Optimal packings of superballs. *Phys. Rev. E*, 79(4):041309, April 2009. doi: 10.1103/PhysRevE.79.041309. URL <http://link.aps.org/doi/10.1103/PhysRevE.79.041309>.
- [45] William Thielicke and Eize Stamhuis. Pivlab towards user-friendly, affordable and accurate digital particle image velocimetry in matlab. *Journal of Open Research Software*, 2(1), October 2014. ISSN 2049-9647. doi: 10.5334/jors.bl. URL <http://openresearchsoftware.metajnl.com/articles/10.5334/jors.bl/>.
- [46] Y. Amarouchene, J. F. Boudet, and H. Kellay. Dynamic sand dunes. *Phys. Rev. Lett.*, 86(19): 4286–4289, May 2001. doi: 10.1103/PhysRevLett.86.4286. URL <http://link.aps.org/doi/10.1103/PhysRevLett.86.4286>.
- [47] C. R. Wassgren, J. A. Cordova, R. Zenit, and A. Karion. Dilute granular flow around an immersed cylinder. *Physics of Fluids (1994-present)*, 15(11):3318–3330, November 2003. ISSN 1070-6631, 1089-7666. doi: 10.1063/1.1608937. URL <http://scitation.aip.org/content/aip/journal/pof2/15/11/10.1063/1.1608937>.
- [48] Peter Knoll, Siroos Mirzaei, and Horst Khn. Numerical simulation of dynamic sand dunes. *Applied Mathematics and Computation*, 190(2):1747–1753, July 2007. ISSN 0096-3003. doi: 10.1016/j.amc.2007.02.115. URL <http://www.sciencedirect.com/science/article/pii/S0096300307002226>.

- [49] John K. Meyer and Robert L. Merlino. Transient bow shock around a cylinder in a supersonic dusty plasma. *Physics of Plasmas (1994-present)*, 20(7):074501, July 2013. ISSN 1070-664X, 1089-7674. doi: 10.1063/1.4812460. URL <http://scitation.aip.org/content/aip/journal/pop/20/7/10.1063/1.4812460>.
- [50] A. Vilquin, J. F. Boudet, and H. Kellay. Structure of velocity distributions in shock waves in granular gases with extension to molecular gases. *Phys. Rev. E*, 94(2):022905, August 2016. doi: 10.1103/PhysRevE.94.022905. URL <http://link.aps.org/doi/10.1103/PhysRevE.94.022905>.
- [51] C. C. Mounfield and S. F. Edwards. A theoretical model for the stress distribution in granular matter. ii. forces in pipes. *Physica A: Statistical Mechanics and its Applications*, 226(1): 12–24, April 1996. ISSN 0378-4371. doi: 10.1016/0378-4371(95)00376-2. URL <http://www.sciencedirect.com/science/article/pii/0378437195003762>.